



Research Paper

Facile synthesis of multi-layer $\text{Co}(\text{OH})_2/\text{CeO}_2\text{-g-C}_3\text{N}_4$ ternary synergistic heterostructure for efficient photocatalytic oxidation of NO under visible light

Zhiyu Xiao^a, Hainam Do^a, Abubakar Yusuf^{a,*}, Hongpeng Jia^b, Haolun Ma^a, Shanshan Jiang^a, Jianrong Li^b, Yong Sun^a, Chengjun Wang^c, Yong Ren^d, George Zheng Chen^e, Jun He^{a,f,**}

^a Department of Chemical and Environmental Engineering, University of Nottingham Ningbo China, Ningbo, PR China

^b Institute of Urban Environment, Chinese Academy of Sciences, Xiamen, PR China

^c College of Resources and Environmental Sciences, South-Central Minzu University, Wuhan, PR China

^d Department of Mechanical, Materials and Manufacturing Engineering, University of Nottingham Ningbo China, PR China

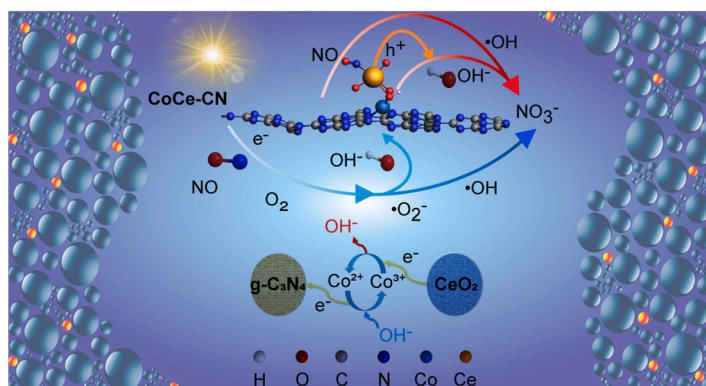
^e Department of Chemical and Environmental Engineering, University of Nottingham, Nottingham, UK

^f Nottingham Ningbo China Beacons of Excellence Research and Innovation Institute, Ningbo, PR China

HIGHLIGHTS

- $\text{Co}(\text{OH})_2$ provides a rapid electron transfer pathway from CeO_2 to $\text{g-C}_3\text{N}_4$.
- $\text{Co}(\text{OH})_2$ as a linker metal hydroxide, enhance the interaction between $\text{g-C}_3\text{N}_4$ and CeO_2 .
- Co-doping of $\text{Co}(\text{OH})_2$ and CeO_2 further improved the photocatalytic efficiency.
- The valence changes of cobalt release more OH^\cdot react with h^+ on the VB of CeO_2 .
- DFT results confirm the multi-layer structure of $\text{Co}(\text{OH})_2/\text{CeO}_2\text{-g-C}_3\text{N}_4$ ternary heterostructure.

GRAPHICAL ABSTRACT



ARTICLE INFO

Editor: Yang Deng

Keywords:

Ternary heterostructure
 $\text{Co}(\text{OH})_2/\text{CeO}_2\text{-g-C}_3\text{N}_4$
 NO photocatalytic oxidation
 Z-scheme heterostructure

ABSTRACT

In this work, we report a one-step synthesis of ternary Z-scheme $\text{Co}(\text{OH})_2/\text{CeO}_2\text{-g-C}_3\text{N}_4$ (CoCe-CN) heterostructure via hydrothermal method. Owing to the modification of $\text{Co}(\text{OH})_2$ and CeO_2 , the existence of $\text{Co}(\text{OH})_2$ as an electron acceptor-donor center between CeO_2 and $\text{g-C}_3\text{N}_4$ accelerates the electron transfer and provides extra OH^\cdot reaction pathway for photocatalytic oxidation of NO. As a result, 50CoCe-CN (Co and Ce accounting for 25% mass ratio separately) achieved a 53.5% conversion efficiency of NO at 600 ppb concentration, which is 1.82 times that of $\text{g-C}_3\text{N}_4$ under visible light. The results of the DFT analysis and element distribution of cobalt and ceria provide convincing evidence supporting the existence of a novel multi-layer structure in the CoCe-CN photocatalyst. This structure involves the loading of CeO_2 and $\text{Co}(\text{OH})_2$ on the $\text{g-C}_3\text{N}_4$ surface, and $\text{Co}(\text{OH})_2$

* Corresponding author.

** Corresponding author at: Department of Chemical and Environmental Engineering, University of Nottingham Ningbo China, Ningbo, PR China.

E-mail addresses: Abubakar.Yusuf@nottingham.edu.cn (A. Yusuf), jun.he@nottingham.edu.cn (J. He).

<https://doi.org/10.1016/j.jhazmat.2023.132744>

Received 10 June 2023; Received in revised form 23 September 2023; Accepted 7 October 2023

Available online 11 October 2023

0304-3894/© 2023 The Author(s). Published by Elsevier B.V. This is an open access article under the CC BY-NC-ND license (<http://creativecommons.org/licenses/by-nc-nd/4.0/>).

as a co-catalyst introduced between CeO_2 and $\text{g-C}_3\text{N}_4$ realizes the synergy between CeO_2 and Co(OH)_2 which further improve the photocatalytic properties. The higher photocatalytic efficiencies observed in the CoCe-CN photocatalysts compared to those containing only cobalt (Co-CN) or ceria (Ce-CN) provide further evidence of the synergistic effect of these two elements. This work demonstrates a more efficient and effective ternary photocatalytic system, with greater practical potential for photocatalytic oxidation of NO.

1. Introduction

Exposure to hazardous indoor air pollution (IAP), such as carbon monoxide (CO), nitrogen oxides (NO_x), particulate matter (PM), and others, is considered a potential long-term hazard to human health, as people spend about 80% of their lifetime indoors [1,2]. Although the concentrations of these indoor air pollutants are sometimes even below the indoor air quality (IAQ) standards at ppb level, long-term exposure and air pollutants accumulation will lead to premature mortality and reduced life expectancy [3-5]. In 2014, the World Health Organization (WHO) reported about 7000,000 premature deaths caused by air pollution, of which 4300,000 were related to IAP. Due to the vast diversity and variability of indoor air pollution, it may lead to various health impacts due to the short- and long-term exposure without effective control.

NO is a harmful air pollutant which leads to tropospheric ozone depletion, the formation of photochemical smog, and acid rain in accumulated high concentrations. It also induces health problems such as pinkeye, respiratory diseases, and lung cancer [6-8]. In the indoor environment, it is usually produced from gas appliances such as stoves, ovens or water heaters, environmental tobacco smoke (ETS), and fireplaces [9-11]. Furthermore, there is a positive correlation between outdoor and indoor NO levels, resulting in an increased indoor NO concentration due to its high outdoor concentration [12]. Consequently, the efficient removal of low concentration indoor NO has become a critical environmental issue in recent years.

Recently, $\text{g-C}_3\text{N}_4$ has been identified as a promising photocatalytic material due to its moderate band gap, good chemical properties, and high stability [13-15]. Moreover, its strong capability for harvesting visible light contributes to its application as an effective photocatalytic material [16]. Owing to its photochemical properties, $\text{g-C}_3\text{N}_4$ is widely studied for low concentration NO photo-oxidation reactions. However, its photocatalytic performance is not particularly high due to its rapid recombination of e^-/h^+ pairs and low specific surface area [17]. To address this challenge and enhance its photocatalytic properties, various methods like chemical modification, element doping, and combination with other semiconductors have been developed [18,19]. Nevertheless, its photocatalytic activity for low concentration NO remains low. For example, $\text{g-C}_3\text{N}_4/\text{SnO}_2$ possesses a Z-scheme heterojunction, leading to an efficient capability to separate and transfer photogenerated carriers. As a result, $\text{g-C}_3\text{N}_4/\text{SnO}_2$ attained about 35% NO photocatalytic efficiency in 30 min under visible light [20]. Therefore, the photocatalytic properties of $\text{g-C}_3\text{N}_4$ based photocatalyst are needed to be improved to enhance its conversion efficiency.

Cerium oxide (CeO_2), as a typical rare earth oxide, has a widespread application as a photocatalytic material owing to its strong oxygen storage capacity, exceptional chemical stability, and stable $\text{Ce}^{3+}/\text{Ce}^{4+}$ redox couple [21]. However, the rapid recombination of its photoelectron hole pairs, and wide bandgap limit its application under visible light. To overcome this limitation, CeO_2 was modified with other materials to form a heterostructure with improved charge separation and reduced the recombination of e^-/h^+ [22-25]. For example, a Flower-like $\text{Bi}^0/\text{CeO}_{2-\delta}$ plasmonic photocatalysts was synthesized to achieve up to 43% photocatalytic NO conversion, 1.7 times as high as that attained by CeO_2 [26]. Despite the improved photocatalytic properties of $\text{Bi}^0/\text{CeO}_{2-\delta}$ compared to CeO_2 , the NO photocatalytic efficiency is still not so high. Consequently, further improvement of e^-/h^+ pairs separation and further suppressing recombination is needed to enhance the

photocatalytic properties of catalysts utilized in NO oxidation, particularly through the manufacturing of ternary heterostructure.

Recently, cobalt has been explored as a photocatalyst owing to its low cost, earth abundance, and p-type property [27]. In addition, cobalt can easily form a p-n heterojunction with n-type photocatalytic materials, resulting in efficient charge separation and inhibited recombination of e^-/h^+ pairs [28]. Among the cobalt-based photocatalysts, Co(OH)_2 is considered as a potential co-catalyst material [29-31], which has stronger adsorption to carrier due to its enhanced separation and transmission of charge carriers and increased charge carrier lifetime by hydroxyl [32].

Ternary heterostructures are a promising class of photocatalysts for NO removal, as they can enhance the light absorption, charge separation and photocatalytic reaction efficiency of single-component or binary photocatalysts [33]. Some examples of ternary heterostructures used in the photocatalytic oxidation of NO are $\text{g-C}_3\text{N}_4 @\text{Ag}/\text{BiVO}_4$ and $\text{TiO}_2/\text{Ag}/\text{Ag}_3\text{PO}_4$ [34,35]. These photocatalysts can achieve high NO conversion rates under visible light irradiation by utilizing Ag as a linker metal or a plasmonic sensitizer or by forming type-II band alignment between different semiconductors. However, silver is known as a noble metal, and its high cost restricts its application in industry or real-life.

This research addresses the issue of the rapid recombination of e^-/h^+ pairs, which hinders NO oxidation under visible light through the formation of a ternary heterostructure photocatalyst. This was achieved by improving the photocatalytic properties of $\text{g-C}_3\text{N}_4$ via its combination with CeO_2 and Co(OH)_2 to construct a p-n type ternary heterojunction. The $\text{CeO}_2/\text{Co(OH)}_2/\text{g-C}_3\text{N}_4$ ternary heterostructure was synthesized by a facile one-step hydrothermal process [36]. In this composition, Co(OH)_2 , as a p-type semiconductor, exists between the surface of CeO_2 and $\text{g-C}_3\text{N}_4$, which not only provides a rapid electron transmission pathway between CeO_2 and $\text{g-C}_3\text{N}_4$ but also further decreases the recombination of e^-/h^+ pairs via the formation of the heterostructure.

2. Materials and Methods

2.1. Preparation of photocatalysts

$\text{g-C}_3\text{N}_4(\text{CN})$: $\text{g-C}_3\text{N}_4$ was prepared based on previous literature as follows [37]: 4 g melamine was placed into a 30 mL alumina crucible with a cover, then heated to 550 °C for 4 h to obtain the final sample. After heating, the resulting powder was grounded for subsequent use.

$\text{Co(OH)}_2/\text{CeO}_2/\text{g-C}_3\text{N}_4$ (CoCe-CN): $\text{Co(OH)}_2/\text{CeO}_2/\text{g-C}_3\text{N}_4$ photocatalysts were synthesized as follows: 0.4 g $\text{g-C}_3\text{N}_4$ was mixed with 180 mL deionized water and 20 mL ethanol. Then the calculated amount of $\text{Co(NO}_3)_3 \cdot 7\text{H}_2\text{O}$ and $\text{Ce(NO}_3)_3 \cdot 7\text{H}_2\text{O}$ were added to the above mixture of $\text{g-C}_3\text{N}_4$ followed by ultrasonication for 10 mins and stirring for 30 mins. Afterwards, 4 mL of 3 mol/L NaOH solution was added in, the mixture of which was sonicated for 5 mins and stirred for 15 mins subsequently. The final solution was then put into a 500 mL autoclave heated at 100 °C for 6 h. After that, the suspension was centrifuged, and washed alternately with deionized water and ethanol until the pH of the mixture was close to 7. Finally, the mixture was dried at 60 °C for 12 h under vacuum. The mass ratios of cobalt and ceria were controlled at 5% Co/5%Ce, 15%Co/15%Ce, 25%Co/25%Ce and 35%Co/35%Ce, and the sample were denoted as $x\text{CoCe-CN}$ (where $x = 10\%, 30\%, 50\%$ and 70%).

$\text{Co(OH)}_2/\text{g-C}_3\text{N}_4$ (Co-CN): The synthesis procedure of $\text{Co(OH)}_2/\text{g-C}_3\text{N}_4$ was the same as described for CoCe-CN above without using Ce

(NO₃)₃•7 H₂O. In order to analyze if there was any synergistic effect between Co and Ce, the mass ratios of Co were controlled at 10% Co, 30% Co, 50% Co, and 70% Co, and designated as *y*Co-CN where *y* represents the mass ratio %.

CeO₂/g-C₃N₄ (Ce-CN): The synthesis procedure of CeO₂/g-C₃N₄ was the same as described for CoCe-CN above without adding Co(NO₃)₃•7 H₂O. The mass ratios of Ce were controlled at 10% Ce, 30% Ce, 50% Ce, and 70%Ce, and designated as *z*Ce-CN where *z* represents the mass ratio %.

Co(OH)₂/CeO₂ (CoCe): The synthesis procedure of Co(OH)₂/CeO₂ was the same as for CoCe-CN above without adding g-C₃N₄, and the sample was taken as CoCe.

2.2. Characterization

The synthesized catalysts were characterized using various techniques using Bruker D8 Advance X-ray diffractometer (XRD) with Cu K α radiation (5°–90°, λ = 1.5406 Å, 40 KV and 40 mA), Scanning electron microscopy (SEM, ZEISS, sigma500, Japan), high-resolution transmission electron microscopy (HRTEM, JEOL, JEM 2100 F, Japan), X-ray photoelectron spectroscopy (XPS, Thermo K-alpha spectrometer, USA), Electron paramagnetic resonance (EPR, Bruker A300, Germany) spectroscopy, UV–vis diffuse reflectance spectroscopy (UV–vis–DRS, Shimadzu UV-3600 +, Japan), Photoluminescence spectrum (PL, HITACHI, F-4600, Japan), and Fourier transform infrared spectroscopy (FT-IR, Nicolet iS5, Thermo, USA). Ion Chromatography (IC, Thermo, ICS 1100, USA). The XPS spectra were calibrated utilizing the C 1 s peak at 284.6 eV on the adventitious carbon surface.

In addition, the Electrochemical impedance spectroscopy (EIS) and Transient photocurrent (TPC) response measurements were employed to determine the electronic properties of photocatalysts. A traditional three-electrode system was setup using an electrochemical workstation (CHI660E, Shanghai Chenhua, China). In this setup, the working electrode, counter electrode, and reference electrode were photocatalyst, Pt electrode, and Ag/AgCl electrode, respectively. The working electrode was prepared by adding 10 mg of catalyst to 1 mL of DI water/ethanol and 50 μ L of Nafion ethanol solution, which was then sonicated for 30 min to form a uniform suspension. The suspension was then transferred to an FTO glass and dried with an infrared lamp at room temperature. During photocurrent response experiments, EIS, and Mott-Schottky tests, a 300 W xenon lamp and the 0.1 mol/L Na₂SO₄ solution were used as the visible-light source and electrolyte, respectively.

To clarify the respective roles of different active species involved in the photocatalytic oxidation of NO, we carried out an active species trapping experiment. We used potassium iodide (KI), potassium dichromate (K₂Cr₂O₇), tert-butanol (TBA), and p-benzoquinone (PBQ) to capture h⁺, e⁻, •OH, and •O₂⁻, respectively.

To evaluate the adsorption capacity of synthesized catalysts, NO adsorption experiment was conducted in a fixed-bed reactor, consisting of a quartz tube column with an inner diameter of 8 mm to be placed in a tube furnace. Prior to the adsorption experiment, 0.1 g of the as-prepared photocatalysts was loaded in the middle of the quartz tube column. The inlet gas mixture contained 200 ppm NO equilibrated with N₂, and the total flow rate was set to 200 mL/min. The reaction temperature for NO oxidation was maintained at room temperature throughout the adsorption experiment. The inlet (C₀) and outlet (C_i) concentrations of NO were measured and recorded using a NO analyzer (Gasboard-3000plus, Hubei). The adsorption capacity (*q*) of NO was calculated using the following equations [38]:

$$q = \frac{FC_0t_q}{W} \quad (1)$$

$$t_q = \int_0^{\infty} \left(1 - \frac{C_i}{C_0}\right) dt \quad (2)$$

where *F* represents the total molar flow (mL/min), *W* is the mass of

photocatalyst loaded in the column (g), and *t_q* is the stoichiometric time (min).

In addition, the NO₃ extraction experiment was conducted on the spent 50CoCe-CN catalyst sample to prove the oxidative conversion of NO to nitrate. In this experiment, two types of duplicate samples were prepared as follows: two portions of 0.1 g of the pristine catalysts (background samples, labelled as B1 and B2) and two portions of used 50CoCe-CN samples (used catalysts, labelled as U1 and U2) were added to four beakers containing 100 mL of deionized water, respectively. After that, B1 and U1 were ultrasonicated for 20 mins and the other two (B2 and U2) were done so for 40 mins, respectively, to extract the NO₃ on the surface of the photocatalysts; thereafter, the powder catalysts were separated by centrifugation and supernatants were collected, from which there were in total four aqueous extract samples (B1–20, B2–40, U1–20, and U2–40). The nitrate concentrations in the aqueous samples were analyzed using Ion Chromatography (IC, Thermo, ICS 1100, USA). The concentration of nitrate converted from NO and deposited on 50CoCe-CN catalysts were calculated by subtracting the nitrate concentrations on B1–20 and B2–40 from those on U1–20 and U2–40, respectively.

The characterization of these catalysts provides valuable information about their structure, morphology, surface electronic states, structural defects, optical properties, and structural vibrations, all of which were utilized to better understand the properties and catalytic mechanism of as-prepared catalysts.

2.3. Catalytic activity test

The activities of synthesized catalysts for NO photocatalytic oxidation were evaluated in a continuous flow cube reactor. The quartz-made reactor was covered with aluminum foil on all sides except for the top (20 × 15 × 10 cm). Before each experiment, 0.2 g prepared catalysts were mixed with 15 mL deionized water, and ultrasonicated for 15 min. Then, the mixture was put into the glass dish with 12 cm diameter and drying at 60 °C for 6 h under vacuum. After that, the glass dish was placed in the center of the cube reactor. To initiate the photocatalytic reaction, a 300 W Xe lamp with a 420 nm cutoff filter was positioned vertically above the catalyst surface (20 cm). During the photocatalytic reaction, 50 ppm NO provided from a compressed gas cylinder (N₂ equilibrium) was diluted by the pure air stream to 600 ppb, which was flowed through the sample surface and the total flow rate in the reactor was 2 L/min. The Xe lamp was turned on to commence the photocatalytic NO oxidation reaction when the adsorption–desorption balance was reached between NO and catalyst. The light intensity, measured using an optical power meter (PL-MW2000, PerfectLight, Beijing) positioned vertically below the lamp at a distance of 20 cm, was 1.516 W. Throughout the entire reaction, the concentrations of NO and NO₂ were measured and recorded by a NO_x analyzer (API-T200, USA) and the photocatalytic efficiency of NO was calculated according to the following equation:

$$\varphi = \frac{C_0 - C}{C_0} \times 100\% \quad (3)$$

where C₀ (ppb) and C (ppb) are NO concentration at the beginning of reaction and given time, respectively.

2.4. Computational details

All the first principles based on density functional theory (DFT) calculations were carried out using the BAND (periodic DFT) module implemented in the Amsterdam modelling suit, which employs localized basis sets (Gaussian and Slater Type Orbitals). The exchange-correlation functional Perdew-Burke-Ernzerhof (PBE) with D4 dispersion energy correction in conjunction with the DZP basis set was employed for the geometry optimization. Before exploring the properties of the CeO₂/Co

(OH)₂/g-C₃N₄, we first optimized and investigated the lattice structure of g-C₃N₄ nanosheets. Geometry optimization calculation is performed using the gradient descent approach with the convergence criterion of 0.001 Hartree/Å for the gradient, 10⁻⁵ Hartree for the potential energy, 0.01 Å for the distance and 0.0005 Hartree stress energy per atom. PBE is known to underestimate the band gap. Therefore, the Heyd-Scuseria-Ernzerhof 2006 (HSE06) hybrid functional was utilized to obtain accurate electronic structure and energy gap of CN, Co, Ce and CoCe-CN photocatalysts. This functional has been widely used for computing the electronic and adsorption properties of 2D materials ([39,40]; P.H.T. Philipsen; [41]).

2. Results and Discussion

2.1. Catalyst characterization

In order to analyze the phase structure of the synthesized catalysts, the crystal structures of CN, Co-CN, Ce-CN and CoCe-CN catalysts were identified by XRD patterns, as shown in Fig. 1(b). The XRD spectra of CN indicate the successful synthesis of a graphite-like carbon nitride phase with two prominent diffraction peaks of 27.4° (0 0 2) and 13.1° (1 0 0), which belong to the stacking of the conjugated aromatic structure and in-plane repeated units, respectively [13,29,30]. The XRD patterns of Ce-CN and Co-CN show obvious peaks ascribed to (0 0 1), (1 0 0), (1 0 1) planes of Co(OH)₂ and (2 0 0), (2 2 0), (3 1 1) planes of CeO₂ [42,43,32, 44-46], all of which confirm that cobalt and ceria were loaded on g-C₃N₄ surface in the form of Co(OH)₂ and CeO₂, respectively. As for CoCe-CN, only the characteristic diffraction patterns of g-C₃N₄, Co(OH)₂ and CeO₂ were observed, indicating the co-existence of cobalt and ceria in g-C₃N₄. All these results consistently indicate that the Co(OH)₂ and CeO₂ were successfully loaded on the g-C₃N₄ surface without destroying their crystal structures.

The structures and chemical functional groups were investigated by FT-IR spectroscopy and depicted in Fig. 1(c). These spectra exhibited broad absorption peaks at 3000–3400 cm⁻¹ that were attributed to the N-H stretching vibration, as well as a variety of peaks at 1239–1641 cm⁻¹ assigned to the aromatic CN heterocyclic ring. The sharp peak at 809 cm⁻¹ was due to the typical vibration of tri-s-triazine units [47,48]. These results revealed that the synthesis of CoCe-CN did not destroy the chemical functional groups and structure of g-C₃N₄. However, distinct peaks attributed to cobalt and ceria were observed in the spectra of Co-CN, Ce-CN and CoCe-CN. The peak centered at 494 cm⁻¹ belongs to the Ce-O bond [49], while the absorption bands at 669 cm⁻¹ and 585 cm⁻¹ are derived from the O-Co-O bridge vibrations and Co-O stretching modes, respectively [50]. Additionally, the typical peak at 3632 cm⁻¹ suggests the presence of Co(OH)₂, matching the XRD results [45,46]. All of these further confirm the successful loading of CeO₂ and Co(OH)₂ on the g-C₃N₄, which are consistent with the XRD results.

The morphological structure and elemental distribution of synthesized catalysts were analyzed using SEM, TEM and energy-dispersive X-ray spectroscopy (EDS) mapping. Fig. S1(a, b) and Fig. S1(c, d) in Supporting Information (SI) illustrate the surface morphologies of the CN and CoCe-CN samples, respectively, revealing the successful combination of Co(OH)₂ and CeO₂ with g-C₃N₄. Additionally, the HRTEM images (Fig. 2(a, b)) demonstrate that the lattice spacing of 0.237 nm and 0.332 nm can be assigned to the (101) plane of Co(OH)₂ and (111) plane of CeO₂ which further confirms the existence of Co(OH)₂ and CeO₂ on the g-C₃N₄ surface [51-54]. EDS element mapping (Fig. 2(c-g)) shows a uniform distribution of C and N on the surfaces of the samples, indicating that g-C₃N₄ is the primary constituent of the catalysts. Moreover, it further confirms the presence of Co and Ce on the surface of g-C₃N₄ in the form of Co(OH)₂ and CeO₂, respectively, as evidenced by the similar distribution of O, Co, and Ce in Fig. 2(c, f, g). Notably, their

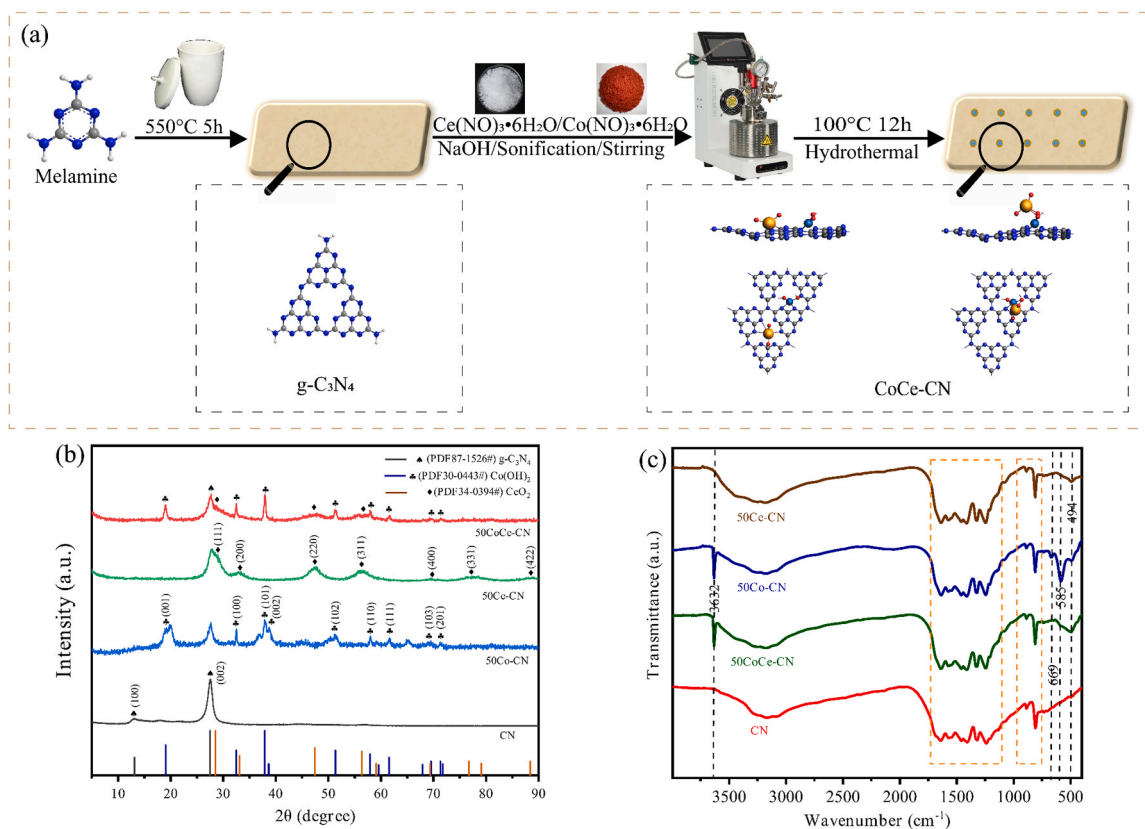


Fig. 1. (a) Schematic illustration for the synthesis of CN and CoCe-CN. (b) XRD patterns and (c) FT-IR spectra of the of CN, Co-CN, Ce-CN and CoCe-CN photocatalysts.

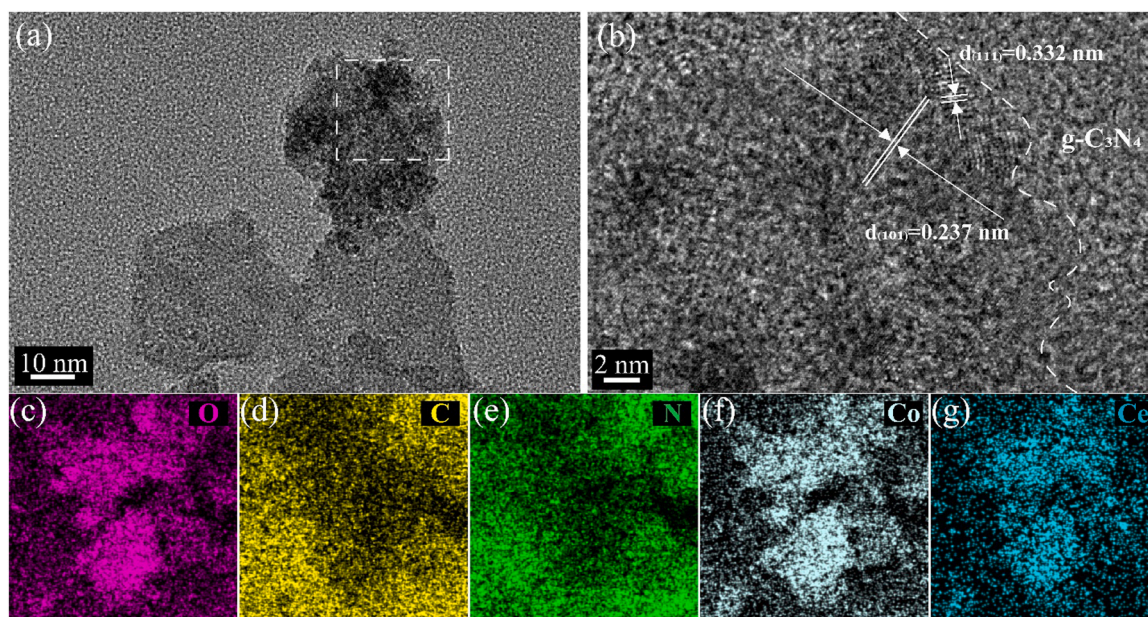


Fig. 2. (a, b) HRTEM images and (c-g) EDS mapping of CoCe-CN.

homogeneous element distribution also indicated an interaction between the Co(OH)_2 and CeO_2 .

The BET result in Table S1 (SI) indicates the mesopores (2–50 nm) existence on the CoCe-CN which is illustrated in Text S1(SI).

The XPS analysis of 50Co-CN, 50Ce-CN and 50CoCe-CN was conducted to investigate the surface element composition and identify the chemical states of $\text{g-C}_3\text{N}_4$, Co and Ce elements in synthesized catalysts. The spectra of $\text{g-C}_3\text{N}_4$ (Fig. 3(a)) reveal two prominent peaks centered at 288.4 eV and 284.8 eV, attributed to sp^2 -bonded carbon (N=C=N) species and sp^3 -bonded carbon (N-C) species, respectively [55–57]. Upon combining $\text{g-C}_3\text{N}_4$ with Co(OH)_2 or CeO_2 , the peak located at 288.4 eV shifted to 288.28 eV or 288.32 eV, respectively. In the case of 50CoCe-CN sample, the peak shifted even further towards lower binding energy (288.06 eV). These results suggest a strong interaction and charge transfer process between Co(OH)_2 , CeO_2 , and $\text{g-C}_3\text{N}_4$, facilitating electron transfer from CeO_2 and Co(OH)_2 to $\text{g-C}_3\text{N}_4$ [32]. Additionally, the interaction between Co and Ce accelerates the electron transfer from them to $\text{g-C}_3\text{N}_4$ due to higher electron density of 50CoCe-CN on the $\text{g-C}_3\text{N}_4$. This finding is further supported by shifts in the N 1s spectra (Fig. 3(b)). Four peaks were observed at 398.8 eV, 400.6 eV, 401.4 eV, and 404.5 eV, corresponding to sp^2 -hybridized aromatic N in C-N=C, tertiary N bonded to N-(C)₃, quaternary N bonded to three carbon atoms in C-N-H and π excitation in heterocycles [55,57]. As observed in Fig. 3 (b), all the corresponding N peaks of CoCe-CN shifted to lower binding energies of 398.6 eV, 399.7 eV, 401.0 eV, and 404.3 eV compared to the $\text{g-C}_3\text{N}_4$ sample. These findings suggest a strong interaction between Co(OH)_2 , CeO_2 , and $\text{g-C}_3\text{N}_4$, leading to electron transfer from the respective loaded materials to $\text{g-C}_3\text{N}_4$.

The Co2p spectrum (Fig. 3(e)) exhibits two prominent peaks centered at 781.1 eV and 796.7 eV ascribed to Co 2p_{3/2} and Co 2p_{1/2}, respectively, as well as two satellite peaks indicating the simultaneous presence of Co^{2+} and Co^{3+} chemical states in Co(OH)_2 [32,45,46]. Comparing the spectra of CoCe and CoCe-CN, a strong interfacial effect is evident due to the coupling of $\text{g-C}_3\text{N}_4$ and $\text{Co(OH)}_2/\text{CeO}_2$, as reflected by the shift of Co 2p peaks towards higher binding energy while the peaks located at 780.43 eV, 785.15 eV, 796.37 eV and 802.07 eV moved to 781.23 eV, 786.09 eV, 796.91 eV and 802.72 eV, respectively [45, 46]. The Ce 3d spectra (Fig. 3(d)) reveal two types of cerium oxidation states simultaneously present, as the characteristic peaks at 916.5, 906.9, 900.7, 898.2, 888.6, and 882.2 eV are ascribed to Ce^{4+} and the peaks at 882.5 and 903.3 eV are attributed to Ce^{3+} 3d_{5/2} and Ce^{3+} 3d_{3/2}

[58,59]. In comparison with CoCe sample, the peaks at 903.8 eV, 906.5 eV, and 915.9 eV in CoCe-CN sample moved to 904.5 eV, 907.6 eV, and 916.6 eV, respectively, which is due to the transfer of electrons from CeO_2 to $\text{g-C}_3\text{N}_4$. Moreover, the peaks at 903.8 eV and 906.5 eV in 50Ce-CN also shift towards higher binding energy when compared with 50CoCe-CN, which indicates the electron transfer between Co(OH)_2 and CeO_2 . As a result, the XPS analysis revealed electron transfer processes between CeO_2 , Co(OH)_2 , and $\text{g-C}_3\text{N}_4$. Specifically, the electron transfer occurs from CeO_2 to Co(OH)_2 and $\text{g-C}_3\text{N}_4$, as well as from Co(OH)_2 to $\text{g-C}_3\text{N}_4$. As for the O 1s region in Fig. 3(c), an asymmetric peak indicates the presence of at least two types of oxygen species [60]. The strongest peak located at 531.0 eV is due to the Co-O-H bond, and the peaks at 529.3 eV and 532.3 eV are ascribed to lattice oxygen of CeO_2 and surface chemisorbed oxygen, respectively [45,46,60].

2.2. Photoelectrochemical properties and band structure

In order to evaluate the absorption performance and the energy bandgap of as-prepared CN, Co(OH)_2 , CeO_2 , 50Co-CN, 50Ce-CN and 50CoCe-CN samples, their UV-vis spectra were obtained via DRS. It is clear from Fig. 4(a) that all the samples have a relatively strong light absorption intensity under visible light. Interestingly, the absorption intensity in the range of 200–800 nm is greatly strengthened after the loading of Cobalt, which is a result of color change due to the presence of Cobalt [29,30,61]. Therefore, it can be concluded that the loading of Co(OH)_2 can apparently enhance the light absorption of the photocatalyst, and that Co(OH)_2 contributes to the observed increased visible light absorption of 50CoCe-CN rather than CeO_2 .

Fluorescence analysis was further conducted to evaluate the separation and recombination of the electron-hole carriers of the photocatalysts. Fig. 4(b) presents the PL spectra of the as-prepared photocatalysts when the excitation wavelength is 419 nm. The strongest PL intensity was observed in the CN sample; however, the intensity decreased upon loading CeO_2 or Co(OH)_2 , implying that both components effectively suppressed electron-hole pair recombination. In addition, the ternary heterostructure formed by the simultaneous incorporation of CeO_2 and Co(OH)_2 further improved the carrier transport and separation properties of the photocatalyst.

The charge separation and recombination for e^-/h^+ pairs at the interface of photocatalysts were further investigated via photocurrent response and EIS, as depicted in Fig. 4(c, d). Our results showed that

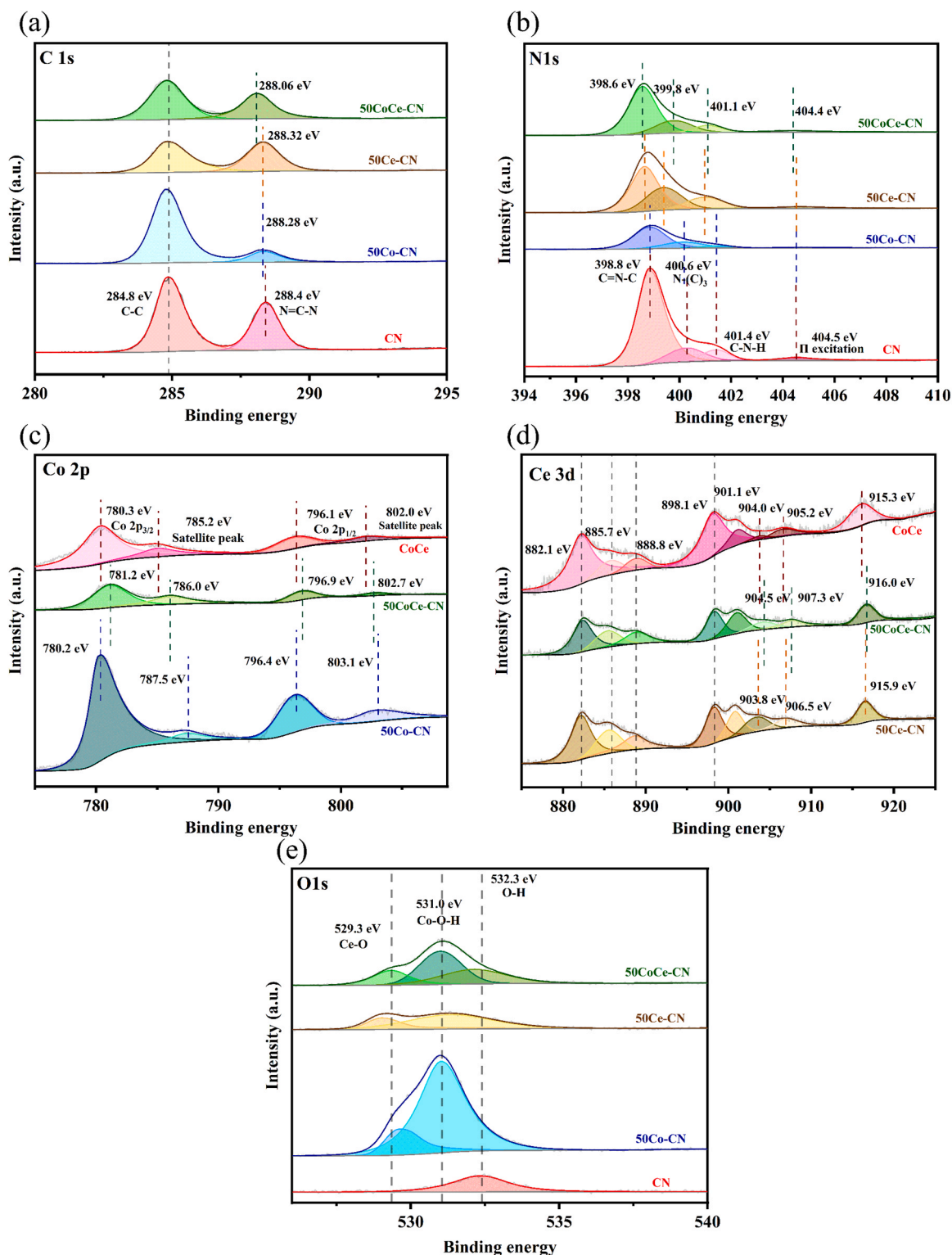


Fig. 3. The XPS spectra of CN, Co-CN, Ce-CN and CoCe-CN photocatalysts. (a)C1s spectra. (b)N1s spectra. (c)O1s spectra. (d)Ce3d spectra. (e) Co2p spectra.

50CoCe-CN possesses the least electrical impedance and more free electrons compared to 50Co-CN and 50Ce-CN, as revealed by the smallest semicircle diameter of all the catalysts in Fig. 4(c). Fig. 4(d) also demonstrates the photocurrent density for each sample under visible light irradiation cycles, suggesting 50CoCe-CN exhibits the strongest photocurrent density that is around 3 ~ and 4 ~ fold as high as 50Co-CN and 50Ce-CN, respectively. Overall, our findings suggest that Co(OH)₂ and CeO₂ inhibit charge carrier recombination and facilitate e⁻/h⁺ pair

separation for g-C₃N₄, and that more improvements of these properties can be achieved by co-loading of g-C₃N₄ with Co(OH)₂ and CeO₂.

In terms of the band structure, the band gaps of the as-prepared samples with a direct band gap were obtained according to the Kubelka-Munk equation:

$$(\alpha h\nu)^{\frac{1}{n}} = A(h\nu - E_g) \quad (4)$$

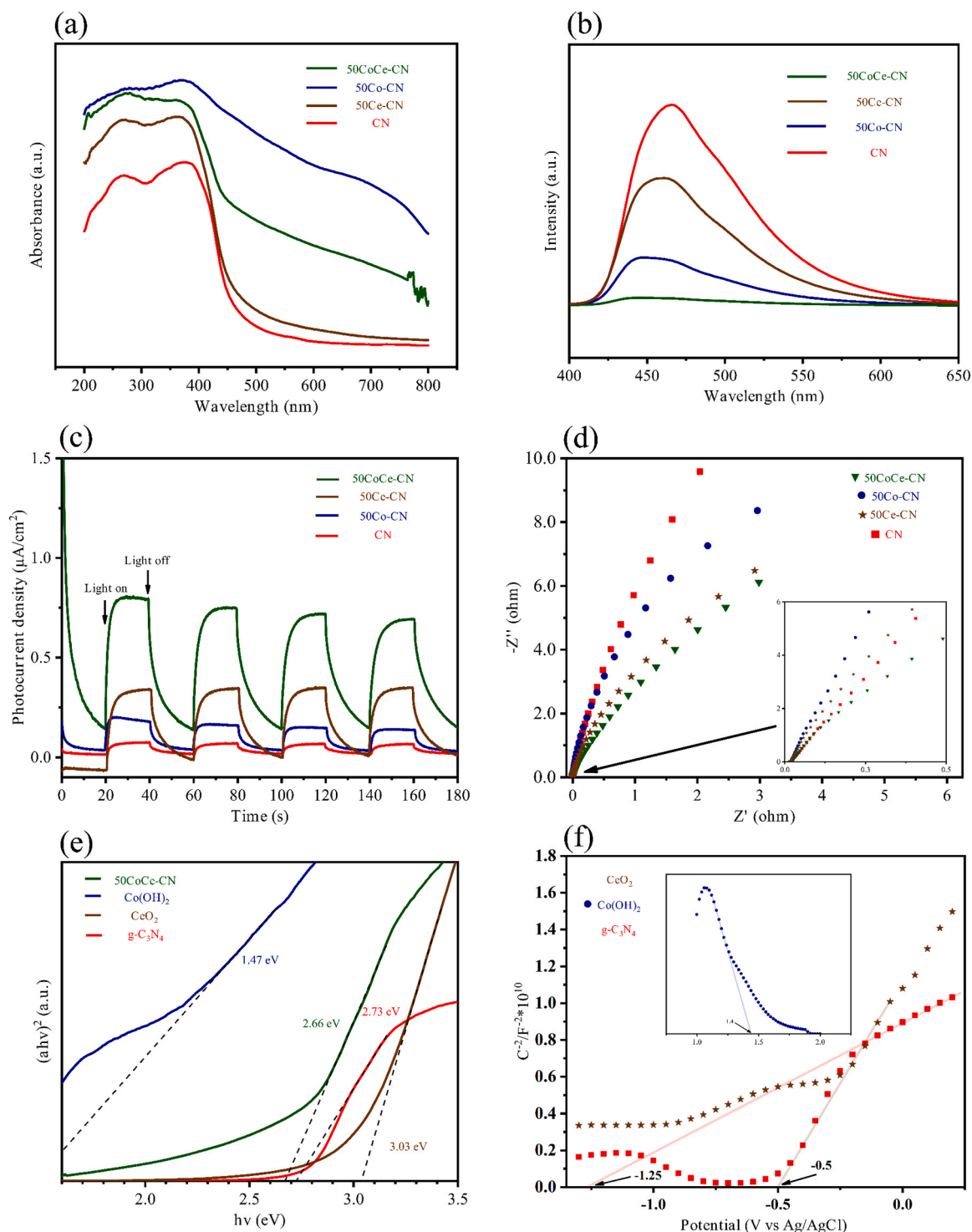


Fig. 4. (a) UV-vis spectra, (b) PL spectra, (c) EIS plots, (d) transient photocurrent responses, (e) Tauc plots and (f) M-S plots of CN, Co-CN, Ce-CN and CoCe-CN photocatalysts.

where α is the optical adsorption coefficient, $h\nu$ represents the absorption energy, E_g is the band gap, and n is equal to $1/2$ for direct band gap materials [62-64]. The band gaps of CN, Co(OH)_2 , CeO_2 and 50CoCe-CN were obtained from the Tauc plots as shown in Fig. 4(e) and estimated to be 2.73 eV, 1.27 eV, 3.03 eV and 2.66 eV, respectively [14,15,10,64, 11]. According to the bandgap result, 50CoCe-CN exhibits a lower bandgap energy compared to CN which facilitates the migration of photogenerated charge carriers between impurity levels and CBs/VBs [65]. The conduction band (CB) was obtained according to

Mott-Schottky plots. From Fig. 4(f), CeO_2 and $\text{g-C}_3\text{N}_4$ exhibit a positive slope of C^{-2} -E plots, indicating CeO_2 and $\text{g-C}_3\text{N}_4$ were attributed to n-type semiconductors. On the contrary, Co(OH)_2 shows a negative slope which means that it belongs to a p-type semiconductor, as expected [66-68]. Therefore, the conduction band edge potentials of $\text{g-C}_3\text{N}_4$ and CeO_2 are -1.25 and -0.5 V vs Ag/AgCl, respectively, and the CBs of $\text{g-C}_3\text{N}_4$ and CeO_2 are -1.19 and -0.44 eV vs reversible hydrogen electrode (RHE), respectively. On the other hand, due to the p-type properties of Co(OH)_2 , the valence band edge potentials of Co

(OH)₂ is 0.13 V vs Ag/AgCl, and the valence bands (VBs) of Co(OH)₂ is 0.19 eV vs RHE. According to the band gap measured from Tauc plots (Fig. 4(e)), VBs of g-C₃N₄ and CeO₂ are 1.54, and 2.59 eV vs RHE, and the CBs of Co(OH)₂ is 1.46 eV vs RHE [14,15,10,11]. To further validate our band analysis, we conducted a valence band X-ray photoelectron spectroscopy (VB-XPS) experiment, as presented in Fig. S2 (SI). The VB positions of CN, Co(OH)₂, and CeO₂ samples were determined by linear extrapolation of the valence band leading edge considering the baseline of the background signal [22–24]. The results revealed VB energies of 1.63 eV, 1.45 eV, and 2.50 eV for CN, Co(OH)₂, and CeO₂, respectively, which are consistent with the findings obtained from the Mott-Schottky analysis.

2.3. Photocatalytic activity tests

To assess the impact of Co(OH)₂ and CeO₂ and their respective mass fractions on the photocatalytic activity, the NO oxidation efficiencies of the photocatalysts were evaluated. The results, as shown in Fig. 5(a), indicate that CN exhibits a relatively low photocatalytic activity with a NO oxidation efficiency of approximately 29.4%. This finding is consistent with previous reports [69,56,20]. However, the introduction of Cobalt and Ceria significantly enhances the NO oxidation efficiency. Furthermore, the NO oxidation efficiency increases with increasing mass fractions of cobalt and ceria, with the best performance observed at mass fractions of up to 25% (50CoCe-CN). Additionally, apart from achieving the highest NO oxidation efficiency of 53.5%, 50CoCe-CN also demonstrates the highest NO₃ selectivity compared to g-C₃N₄, as depicted in Fig. 5(b). Further increasing the loading ratios of Co(OH)₂ and CeO₂ resulted in a decreased NO oxidation efficiency due to particle

aggregation and blockage of active sites by excessive Co(OH)₂ and CeO₂. This indicates that the mass fraction of loaded material is an essential factor that impacts the photocatalytic oxidation of NO by photocatalysis. Consequently, 50CoCe-CN exhibits relatively high efficiency in the photocatalytic oxidation of NO when comparing with previous research, demonstrated in Table 1.

In order to confirm the synergistic effect of cobalt and ceria on g-C₃N₄, the photocatalytic activities of Co-CN and Ce-CN were investigated and shown in Fig. 5(c). It can be seen that 50Co-CN and 50Ce-CN achieved 39.5% and 43.9% NO oxidation efficiency, respectively, which are less than that of 50CoCe-CN (53.5%). This indicates that the interaction between cobalt and ceria is consistent with the photoelectrochemical characterization results, which further improved the oxidation efficiency of NO. To demonstrate the stability of the photocatalyst, the oxidation tests of five cycles with 120 mins per cycle was carried out. The stability test results depicted in Fig. 6(a) showed the long-lasting photocatalytic performance achieved by the 50CoCe-CN. Additionally, the new XRD results were acquired for the used 50CoCe-CN samples, as shown in Fig. 6(b). These results consistently indicate that the crystal and morphological structures were preserved after 600 mins test, which confirms the good stability of the 50CoCe-CN photocatalyst.

2.4. DFT analysis

The multi-layer structure of CoCe-CN was confirmed by the result of geometry optimization calculation, as described in Text S2 (SI). To assess the adsorption behavior of NO on a multi-layer CoCe-CN structure, the structure in Fig. S2 (e, f) was employed to simulate NO

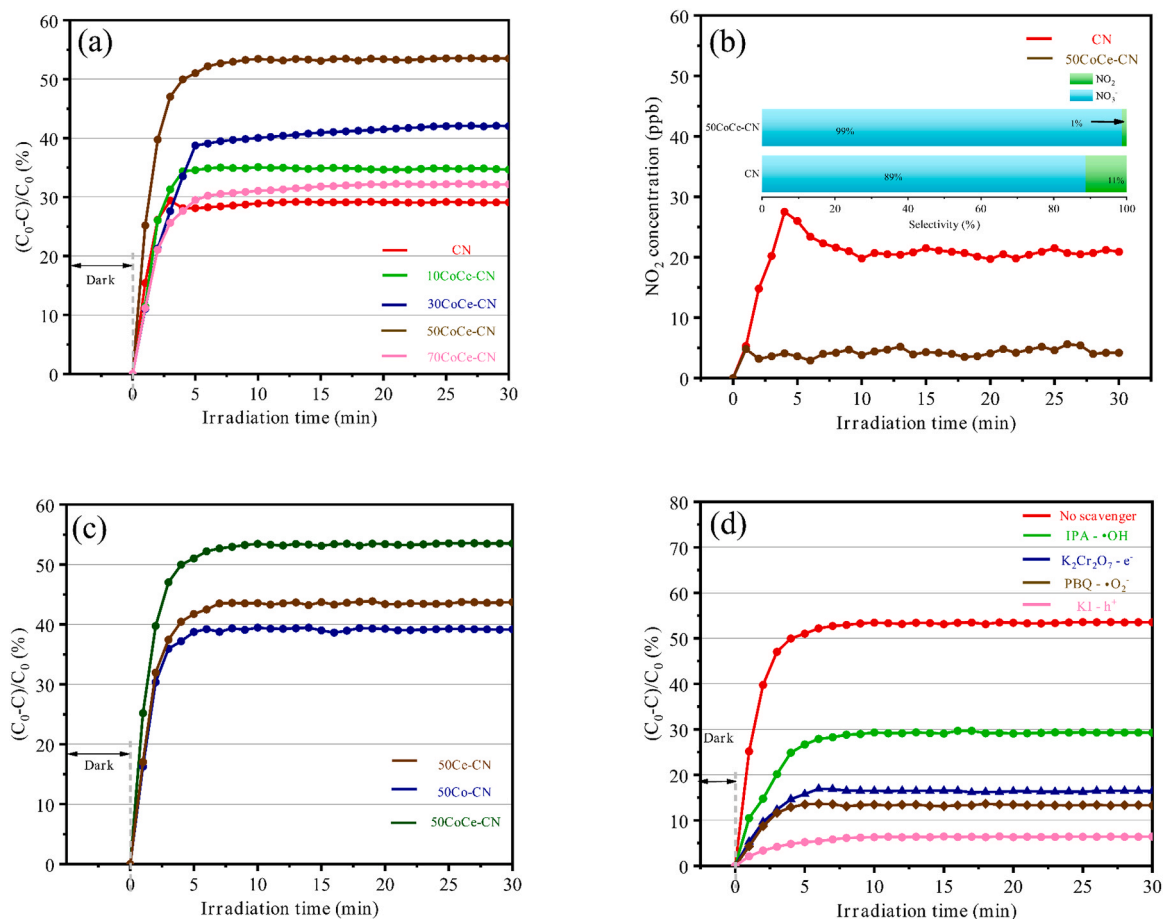


Fig. 5. (a) Conversion of NO for 10/30/50/70CoCe-CN and CN, (b) concentration of NO₂ and selectivity for CN and 50CoCe-CN, (c) Conversion of NO of 50Co-CN, 50Ce-CN and 50CoCe-CN and (d) The capture experiments for photocatalytic removal NO of CoCe-CN.

Table 1
Comparison of NO photocatalytic efficiency.

Photocatalyst	Catalyst dosage/mg	Initial NO concentration ppb	Light source	Efficiency %	Year	Reference
50CoCe-CN	200	600	300 W Xe lamp	53	2023	This study
CaCO ₃ /g-C ₃ N ₄	200	550	LED lamp	51.18	2023	[70–73]
CQD-OVTNs	75	1000	500 W Xe lamp	57.8	2023	[70–73]
Au/Bi ₄ Ti ₃ O ₁₂	100	430	300 W Xe lamp	48	2023	[14,15]
BrGLx	200	550	LED lamp	48.2	2023	[70–73]
O-g-C ₃ N ₄ @W ₁₈ O ₄₉	100	500	300 W Xe lamp	56.7	2023	[70–73]
CNN-S	200	600	150 W LED lamp	53	2023	[74]
STO-SCO	100	400	300 W Xe lamp	44	2023	[42,43]
Bi/BiOBr	50	800	300 W Xe lamp	63	2023	[75]

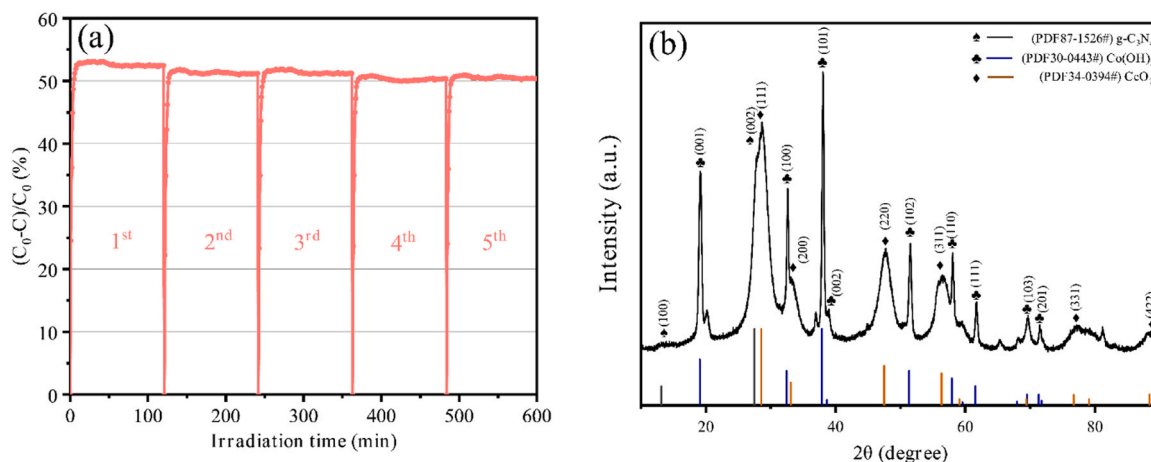


Fig. 6. (a) stability of 50CoCe-CN for five repeated photocatalytic runs and (b) XRD result of used photocatalyst.

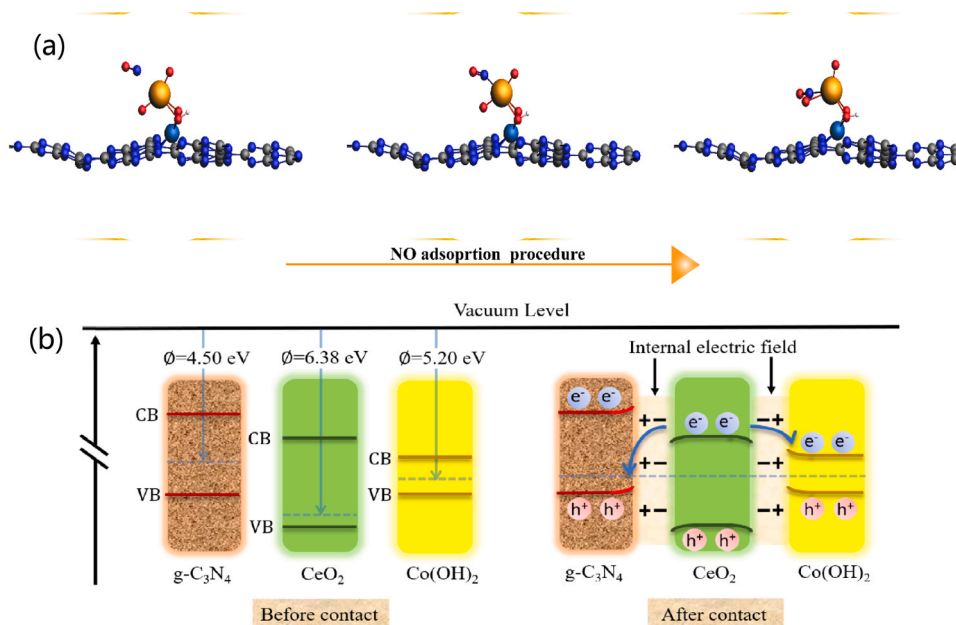


Fig. 7. (a) Schematic illustration for NO adsorption on CoCe-CN and (b) photogenerated electron transfer before and after contact.

adsorption. Fig. 7(a) displays the spontaneous adsorption process of NO on CoCe-CN photocatalyst, implying that CeO₂ possesses a stronger adsorption energy towards NO in comparison with g-C₃N₄. Consequently, a high concentration of NO adsorbed on CeO₂ was oxidized by •OH or h⁺ during the photocatalytic oxidation reaction. This finding is constituent with the trapping experiments, which suggest that h⁺ is the most crucial active species in photocatalytic oxidation of NO. To

evaluate the electron transfer pathway in CoCe-CN composites, the bandgap and work function of CN, Co(OH)₂ and CeO₂ are analyzed, and the calculated details are shown in Text S3 (SI). From Fig. 7(b), the work functions of g-C₃N₄, CeO₂ and Co(OH)₂ are calculated as 6.38 eV, 4.50 eV and 5.20 eV, respectively. Consequently, due to the disparity in their Fermi levels, electrons will transfer from CeO₂ to g-C₃N₄ and Co(OH)₂ until equilibrium levels are achieved. This process results in the

accumulation of photogenerated electrons on g-C₃N₄ and Co(OH)₂ and holes on CeO₂, respectively, effectively creating the internal electric field (IEF) which is shown in Fig. 7(b) [76-81]. Consequently, it caused the thermodynamically transfer of electrons from CeO₂ to g-C₃N₄ and Co(OH)₂, which are consistent with our XPS results discussed in Section 2.1.

The charge density difference (CDD) calculation is a useful tool that can be used to describe the redistribution of charge that occurs due to the formation of heterojunctions. The formula for CDD is similar to that for adsorption energy, and it can be expressed as:

$$\rho_{\text{ad}} = \rho_{\text{gas-sub}} - \rho_{\text{sub}} - \rho_{\text{gas}} \quad (5)$$

CDD can be defined as the difference in the total electron density of the combined adsorbent and adsorbent system, and the densities of the isolated adsorbent and adsorbent system. In Fig. 8, the blue distribution represents electron accumulation, while the yellow distribution represents electron depletion. Thus, electrons flow from the yellow regions to the blue regions. The isosurface is taken as 0.003 a.u. From Fig. 8, a significant number of yellow regions are observed at the bottom of CeO₂, indicating electron loss for all the CeO₂ samples. In Fig. 8(c, d), Co(OH)₂ is located between CeO₂ and the surface. The portion of Co(OH)₂ near CeO₂ is enveloped by blue regions, indicating the flow of electrons from CeO₂ to Co(OH)₂. Additionally, a significant number of yellow regions are present at the bottom of cobalt, suggesting electron flow towards the g-C₃N₄ surface. Regardless of the involvement of cobalt, the surface of g-C₃N₄ is abundantly populated with blue regions, indicating that after the formation of heterojunctions, electrons are enriched on the surface of g-C₃N₄. All the figures depict the flow of electrons from 0-dimensional (CeO₂ and Co(OH)₂) materials to the surface of g-C₃N₄. However, in Fig. 8(c, d), the blue regions on the surface of g-C₃N₄ are noticeably larger and more abundant compared to Fig. 8(a, b). This indicates that the involvement of Co(OH)₂ significantly enhances the quantity of electrons enriched on the surface of g-C₃N₄. Therefore, the result of CDD calculation confirms that the existence of Co(OH)₂ between CeO₂ and g-C₃N₄ further accelerates the electron transfer from CeO₂ to g-C₃N₄.

2.5. NO photocatalytic oxidation mechanism

To further elucidate the photocatalytic mechanism for photocatalytic

oxidation of NO, this study investigated the contributions of different active species by introducing scavenger agents to trap them. Results in Fig. 5(d) demonstrate that the efficiency of photocatalytic oxidation of NO significantly declined when PBQ, KI, and K₂Cr₂O₇ were added, indicating that •O₂⁻, h⁺ and e⁻ species are critical for the photocatalytic reaction. In addition, photodegradation of NO exhibited relatively weak inhibitory effects with the presence of TBA used for trapping •OH, indicating that the contribution of •OH is secondary in this process. Additionally, a NO₃⁻ extraction experiment by ultrasonication and Ion Chromatography was conducted to prove the photocatalytic oxidation of NO to NO₃⁻ by 50CoCe-CN photocatalyst. As shown in Fig. S5 (SI), the net NO₃⁻ concentrations in the aqueous extracts from U1-20 and U1-40 can be up to 40.7 and 110.02 mg/L, respectively, confirming the effective conversion of NO to NO₃⁻ during the photocatalytic reaction.

The adsorption capacity of NO is also a crucial factor that influences the efficiency of photocatalytic oxidation. It directly affects the quantity of NO molecules that can be adsorbed onto the active sites of the photocatalyst during the photocatalytic reaction. The results of the NO adsorption experiment are depicted in Fig. 9. Among the samples tested, CN exhibited the poorest NO adsorption capacity, with a value of only 23.17 mg/g. However, the introduction of Co or Ce significantly improved the NO adsorption capacity. Furthermore, 50CoCe-CN demonstrated a superior NO adsorption capacity compared to 50Co-CN and 50Ce-CN, indicating that the co-loading of Co and Ce further enhanced the NO adsorption capacity, which resulted in a greater amount of NO to be adsorbed on the surface of the photocatalyst so as to increase the photocatalytic oxidation efficiency of NO.

The EPR results were utilized to assess the production of •O₂⁻ and •OH radicals during the photocatalytic oxidation of NO. From the EPR profiles as presented in Fig. 10(b), no obvious characteristic peaks were observed in all samples under the dark condition. However, after 10 mins of illumination under visible light, all the samples displayed peaks with intensity ratios of 1:2:2:1 and 1:1:1:1, which are ascribed to •OH/DMPO and •O₂⁻, respectively [22-24]. In this case, g-C₃N₄ exhibits the lowest EPR peak intensity, while the spectra intensity gradually increases after the loading of Co and Ce. This suggests that g-C₃N₄ has the poorest ability to generate photogenerated electrons during the photocatalytic oxidation of NO, resulting in minimal conversion of oxygen to •O₂⁻. However, the loading of either Co or Ce enhances the electron transfer and suppresses recombination of photogenerated

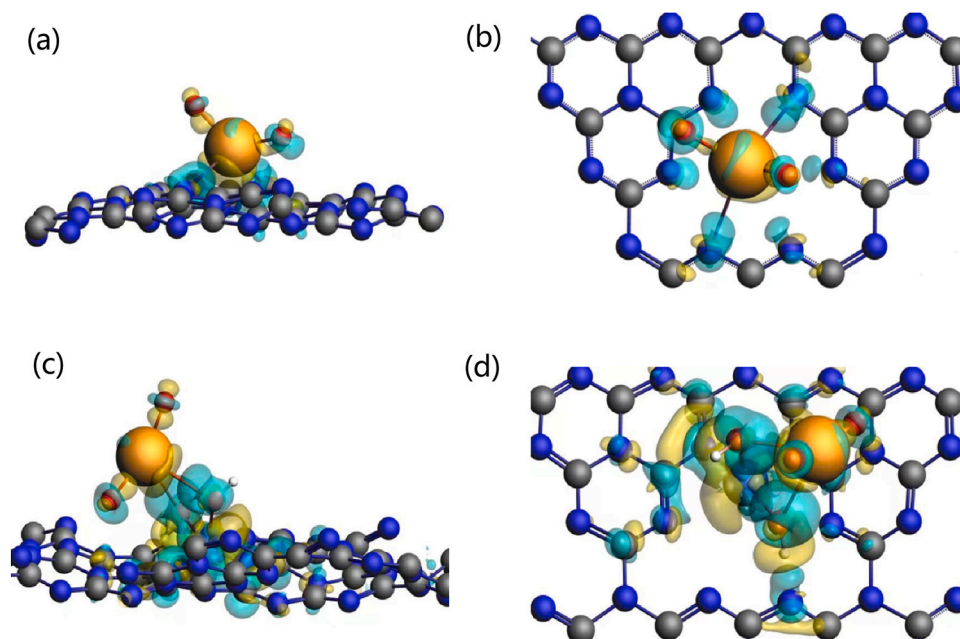


Fig. 8. Charge density differences of (a, b) Ce-CN and (c, d) CoCe-CN.

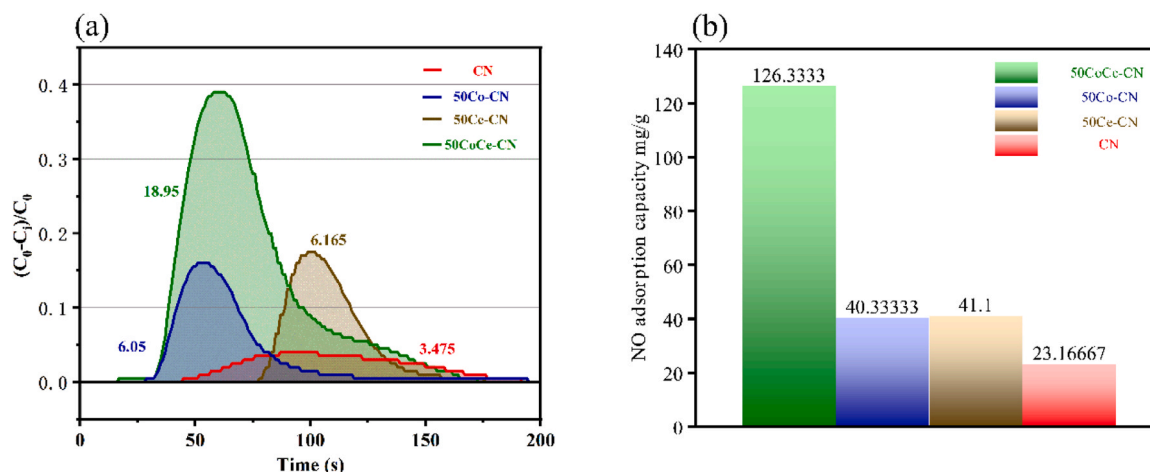


Fig. 9. (a) NO adsorption curves and (b) NO adsorption capacity of CN, 50Co-CN, 50Ce-CN and 50CoCe-CN sample.

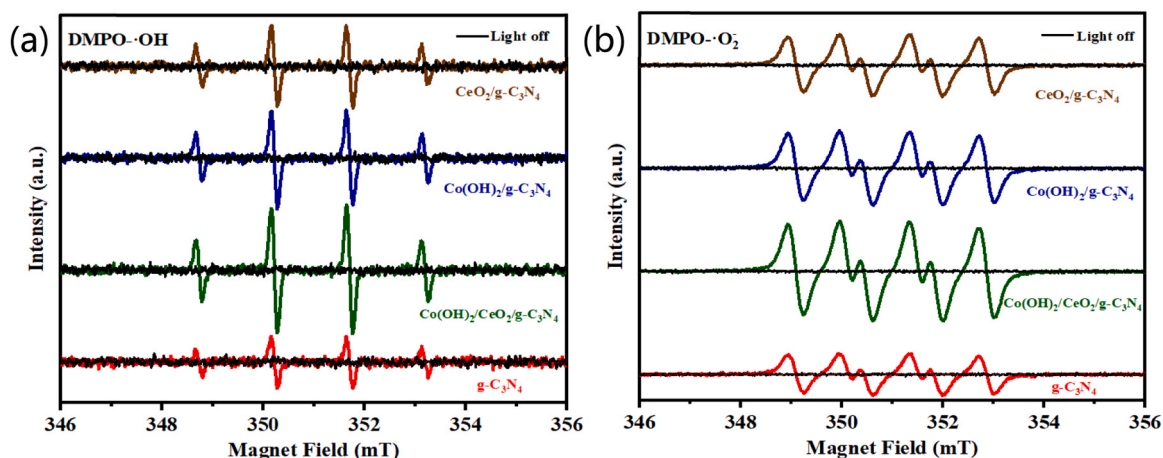


Fig. 10. Intensity of •OH (a) and •O₂ (b) generated by CN, Co-CN, Ce-CN and CoCe-CN under visible light irradiation by EPR.

electrons and holes, thereby improving the production of •O₂. Furthermore, 50CoCe-CN demonstrates the strongest peak intensity, indicating that the synergistic interaction between Co(OH)₂ and CeO₂ further accelerates the production of •OH and •O₂ (as shown in Fig. 10), resulting in enhanced NO oxidation during the photocatalytic reactions. It implies that the co-loading of Co(OH)₂ and CeO₂ led to the construction of ternary heterojunctions between g-C₃N₄, Co(OH)₂ and CeO₂, which on the other hand, enhanced the separation efficiency and weakened the recombination of e⁻/h⁺. The ternary heterojunctions resulted in more photo-generated e⁻/h⁺ to participate in photocatalytic reactions than the binary photocatalysts (Co-CN and Ce-CN), in agreement with the photo-electrochemical results discussed earlier.

This study proposes a pathway for electron transport between ternary heterojunctions based on the band structure of CoCe-CN and DFT results, as discussed in the DFT Section and presented in Fig. 6(b). The transferred electrons flow from CeO₂ and Co(OH)₂ towards g-C₃N₄, and from CeO₂ towards Co(OH)₂, leading to the creation of an interface electric field and ternary heterojunction. Consequently, the photo-generated electrons in the CB of CeO₂ migrate to the CB of Co(OH)₂. Likewise, the photo-generated electrons in the CB of Co(OH)₂ can transfer to the VB of g-C₃N₄. Subsequently, the transferred photo-generated electrons from the CB of CeO₂ and Co(OH)₂ combine with the photo-generated holes accumulated in the VB of g-C₃N₄, resulting in the formation of a ternary Z-scheme heterojunction between g-C₃N₄, CeO₂, and Co(OH)₂. This heterojunction improves the electron transfer efficiency and provides a higher VB potential and lower CB potential. The

transport pathway for photogenerated charge carriers can also be inferred from the EPR result. Unlike the classic type II heterojunction photocatalyst, where the photogenerated electrons in the CB of g-C₃N₄ and Co(OH)₂ are induced to the CB of Co(OH)₂ and VB of CeO₂, respectively, in this case, the holes of g-C₃N₄ possess an insufficient potential energy of 1.46 V vs RHE to oxidize H₂O and OH⁻ to •OH. Consequently, less •OH is produced, contradicting the EPR results. Thus, the type II mechanism does not adequately explain the NO oxidation by the CoCe-CN heterojunction. During the photocatalytic reaction, Co(OH)₂ acts as a special intermediate between g-C₃N₄ and CeO₂. Firstly, Co(OH)₂ possesses a low bandgap, which leads to high light absorption for CoCe-CN. Additionally, it can act as an electron donor-acceptor between g-C₃N₄ and CeO₂ due to its rapid recombination and production of e⁻/h⁺ pairs, as well as its p-type properties. Thirdly, valence changes of cobalt occur during electron transfer through Co(OH)₂, which results in the release and acceptance of OH⁻. The mechanism of Co(OH)₂ can be illustrated in Fig. 11(a). The presence of Co(OH)₂ enhances the light absorption of CoCe-CN and accelerates the electron transfer between CeO₂ and g-C₃N₄. During the photocatalytic reaction, the electron from the CB of CeO₂ initially transfers to the CB of Co(OH)₂, and subsequently, the electron on the CB of Co(OH)₂ transfers to the VB of g-C₃N₄. The step-by-step transfer of electrons reduces the energy barrier of electron transfer and promotes electronic communication between CeO₂ and g-C₃N₄. During the electron transfer from CeO₂ to Co(OH)₂, the valence of cobalt decreases from +3 to +2 with the release of OH⁻. The released OH⁻ then participates in the reaction on the VB of CeO₂ to form

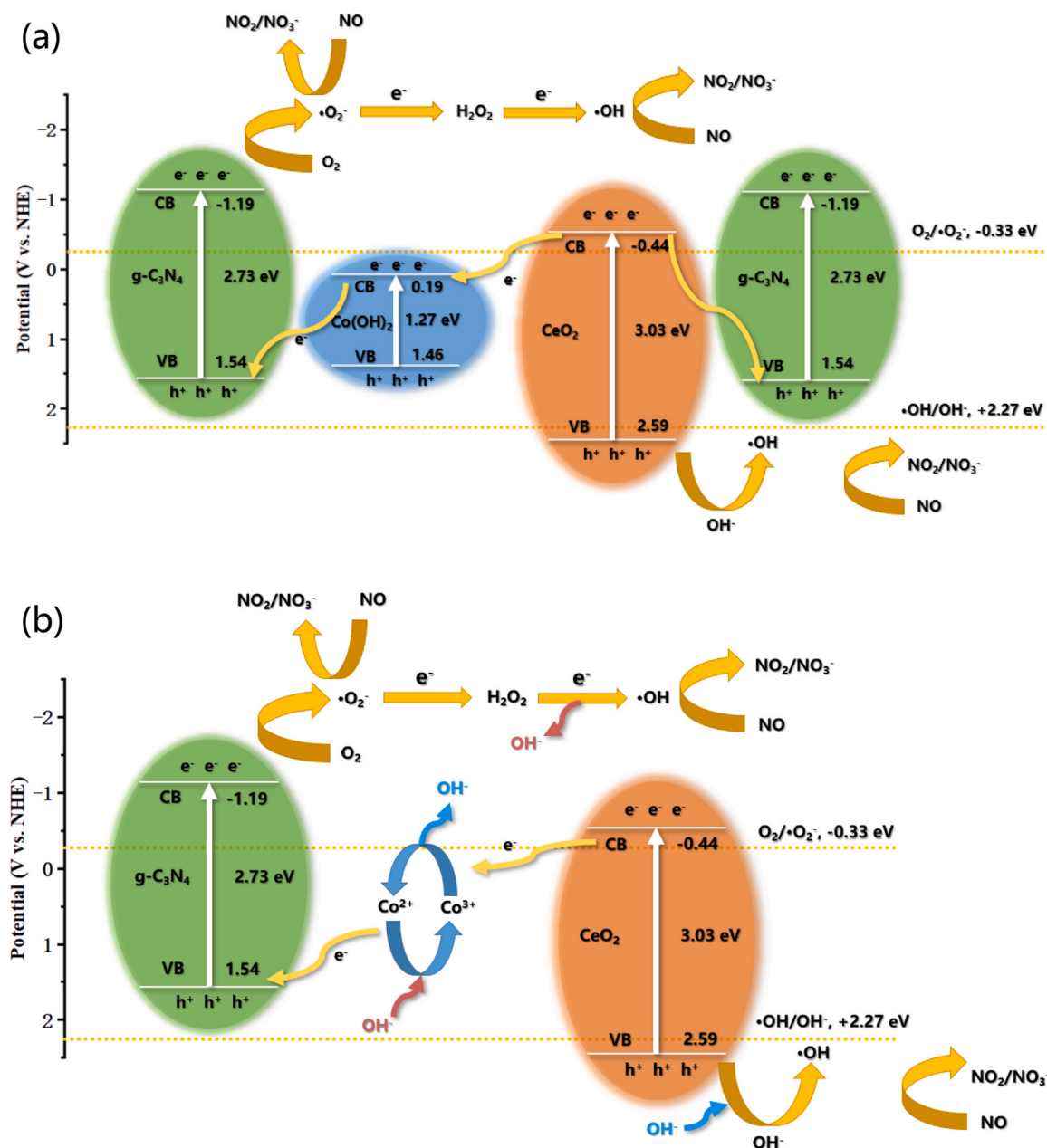
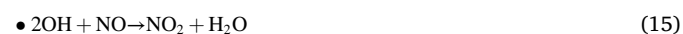
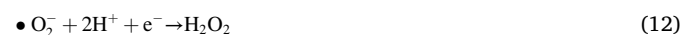
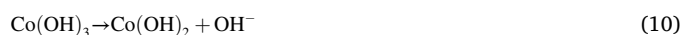


Fig. 11. Photocatalytic reaction mechanism of CoCe-CN ternary heterojunction based on the Z-scheme interface for NO oxidation under visible light.

•OH. Afterwards, the electron on the CB of Co(OH)_2 transfers to the VB of $\text{g-C}_3\text{N}_4$ with an increased valence of cobalt from +2 to +3. The electron on the CB of $\text{g-C}_3\text{N}_4$ reacts with H_2O_2 to produce OH^- , which can react with Co^{3+} to form Co(OH)_3 . This mechanism indicates that the valence change of cobalt also provides OH^- to participate in the photocatalytic reaction.

According to the Z-scheme mechanism, the electron will react with O_2 in the CB of $\text{g-C}_3\text{N}_4$ to form $\bullet\text{O}_2^-$, which further reacts to generate $\bullet\text{OH}$ via H_2O_2 intermediates. Then, the oxidized radicals will react with adsorbed NO to form NO_2/NO_3 . On the other hand, due to the relatively higher potentials of the photogenerated holes in the VB of CeO_2 , it can directly oxidize NO to NO_2/NO_3 and react with $\text{H}_2\text{O}/\text{OH}^-$ to form $\bullet\text{OH}$, as illustrated in Fig. 11(b). According to the discussions above, the mechanism for NO photocatalytic oxidation by CoCe-CN photocatalyst can be illustrated by the following chemical reactions:





4. Conclusions

In this work, CoCe-CN ternary Z-scheme heterostructure was successfully synthesized by a one-step hydrothermal process and proven to be an effective photocatalyst for NO oxidation. The fabrication of ternary Z-scheme heterostructure further improves the separation and inhibits the recombination of electron-hole pairs. Consequently, up to 53.5% photocatalytic oxidation of NO was achieved from the starting concentration of 600 ppb when the respective mass fractions of cobalt and ceria were 25% (50CoCe-CN). However, further increasing the respective mass fractions of cobalt and ceria beyond 25% led to a decrease in NO oxidation efficiency due to particle aggregation and blockage of active sites by extra oxides. Furthermore, the synthesized catalysts possess high selectivity for NO₃⁻ compared with g-C₃N₄, and displayed good stability and recyclability as verified by recycling tests. This work has presented a practical one-pot approach for synthesizing ternary Z-scheme heterostructure photocatalysts for NO oxidation, which demonstrates the superior photocatalytic properties of ternary heterostructure than binary heterostructure and offers new insights for the preparation of other ternary heterostructure photocatalytic materials.

Environmental Implication

NO_x is considered as a harmful air pollutant in both outdoor and indoor environments, which can lead to photochemical smog and cause respiratory diseases via the exposure. Herein, a ternary heterostructure Co(OH)₂/CeO₂-g-C₃N₄ photocatalyst was fabricated using a facile ultrasonication-hydrothermal process which was found to improve the oxidation efficiency up to 53% at the NO concentration down to ppb level. In this photocatalyst of multi-layer structure, Co(OH)₂ not only promotes the electronic communication between g-C₃N₄ and CeO₂, but also provides an efficient pathway to utilize OH⁻ to accelerate the production of •O₂⁻ and •OH.

CRedit authorship contribution statement

Zhiyu Xiao: Investigation, Data curation, Writing – original draft, Writing – review & editing. **Hainam Do, Haolun Ma, Shanshan Jiang:** Investigation, Methodology, Data curation. **Abubakar Yusuf, Hongpeng Jia, Jianrong Li, Chengjun Wang, Yong Ren, George Zheng Chen:** Methodology, Writing – review & editing. **Yong Sun:** Supervision, Writing-review & editing, Funding acquisition. **Jun He:** Funding acquisition, Supervision, Project administration, Writing – review & editing.

Declaration of Competing Interest

The authors declare the following financial interests/personal relationships which may be considered as potential competing interests: Jun He reports financial support was provided by Ningbo Science and Technology Bureau.

Data Availability

Data will be made available on request.

Acknowledgements

This work was jointly sponsored by the Ningbo Science and Technology Innovation Key Projects (Nos. 2020Z099, 2022Z028), Natural Science Foundation Key Project from Ningbo Bureau of Science and Technology (2023J024), Ningbo Commonweal Key Research Program

(2023S038), Li Dak Sun Fellowship from University of Nottingham Ningbo China (E06211200005) and the engagement project from Nottingham Ningbo China Beacons of Excellence Research and Innovation Institute.

Appendix A. Supporting Information

BET surface area and pore size distribution, SEM images, Band structure obtained by DFT calculations and optimized photocatalyst structure are included in the Supporting Information.

Appendix A. Supporting information

Supplementary data associated with this article can be found in the online version at [doi:10.1016/j.jhazmat.2023.132744](https://doi.org/10.1016/j.jhazmat.2023.132744).

References

- [1] Fleck, R., Gill, R.L., Pettit, T., Irga, P.J., Williams, N.L.R., Seymour, J.R., et al., 2020. Characterisation of fungal and bacterial dynamics in an active green wall used for indoor air pollutant removal. *Build Environ* 179, 106987. <https://doi.org/10.1016/j.buildenv.2020.106987>.
- [2] Tran, V.V., Park, D., Lee, Y.C., 2020. *Indoor Air Pollution, Related Human Diseases, and Recent Trends in the Control and Improvement of Indoor Air Quality*. *Int J Environ Res Public Health* 17 (8), 2927.
- [3] Chung, C.Y., Yang, J., He, J., Yang, X., Hubbard, R., Ji, D., 2021. An investigation into the impact of variations of ambient air pollution and meteorological factors on lung cancer mortality in Yangtze River Delta. *Sci Total Environ* 779, 146427. <https://doi.org/10.1016/j.scitotenv.2021.146427>.
- [4] Kampa, M., Castanas, E., 2008. Human health effects of air pollution. *Environ Pollut* 151 (2), 362–367. <https://doi.org/10.1016/j.envpol.2007.06.012>.
- [5] Xu, J., Tai, X., Betha, R., He, J., Balasubramanian, R., 2015. Comparison of physical and chemical properties of ambient aerosols during the 2009 haze and non-haze periods in Southeast Asia. *Environ Geochem Health* 37 (5), 831–841. <https://doi.org/10.1007/s10653-014-9667-7>.
- [6] Khan, M.S., Priyadarshini, M., Bano, B., 2009. Preventive Effect of Curcumin and Quercetin against Nitric Oxide Mediated Modification of Goat Lung Cystatin. *J Agric Food Chem* 57 (14), 6055–6059. <https://doi.org/10.1021/jf900356w>.
- [7] Lee, E.K., Romeiko, X.X., Zhang, W., Feingold, B.J., Khwaja, H.A., Zhang, X., et al., 2021. Residential Proximity to Biorefinery Sources of Air Pollution and Respiratory Diseases in New York State. *Environ Sci Technol* 55 (14), 10035–10045. <https://doi.org/10.1021/acs.est.1c00698>.
- [8] Xu, J.S., Xu, H.H., Xiao, H., Tong, L., Snape, C.E., Wang, C.J., et al., 2016. Aerosol composition and sources during high and low pollution periods in Ningbo, China. *Atmos Res* 178–179, 559–569. <https://doi.org/10.1016/j.atmosres.2016.05.006>.
- [9] Rafeeq, H., Zia, M.A., Hussain, A., Bilal, M., Iqbal, H.M.N., 2022. Indoor air pollution and treatment strategies—Hybrid catalysis and biological processes to treat volatile organic compounds. In: Assadi, A., Amrane, A., Nguyen, T.A. (Eds.), *Hybrid and Combined Processes for Air Pollution Control*. Elsevier, pp. 257–283. <https://doi.org/10.1016/B978-0-323-88449-5.00003-6>.
- [10] Wang, H., Sun, Y., Dong, F., 2022. Insight into the Overlooked Photochemical Decomposition of Atmospheric Surface Nitrates Triggered by Visible Light. *Angew Chem Int Ed* 61 (43), e202209201. <https://doi.org/10.1002/anie.202209201>.
- [11] Wang, X., Li, Y., Guo, X., Jin, Z., 2022. In Situ Synthesis of Ag/Ag₂O on CeO₂ for Boosting Electron Transfer in Photocatalytic Hydrogen Production. *J Phys Chem C* 126 (31), 13015–13024. <https://doi.org/10.1021/acs.jpcc.2c03411>.
- [12] Silvia, Ve, 2011. Indoor Nitrogen Oxides, in: Farhad, N. (Ed.) *Advanced Air Pollution*. IntechOpen, Rijeka, p. Ch. 3. <https://doi.org/10.5772/16819>.
- [13] Du, L., Gao, B., Xu, S., Xu, Q., 2023. Strong ferromagnetism of g-C₃N₄ achieved by atomic manipulation. *Nat Commun* 14 (1), 2278. <https://doi.org/10.1038/s41467-023-38012-8>.
- [14] Liu, L.L., Chen, F., Wu, J.H., Chen, J.J., Yu, H.Q., 2023. Synergy of crystallinity modulation and intercalation engineering in carbon nitride for boosted H₂O₂ photosynthesis. *Proc Natl Acad Sci* 120 (6), e2215305120. <https://doi.org/10.1073/pnas.2215305120>.
- [15] Liu, Z., An, Y., Zhang, W., Zhu, L., Zhu, G., 2023. Au nanoparticles modified oxygen-vacancies-rich Bi₄Ti₃O₁₂ heterojunction for efficient photocatalytic NO removal with high selectivity. *J Alloy Compd* 942, 169018. <https://doi.org/10.1016/j.jallcom.2023.169018>.
- [16] Gao, G., Jiao, Y., Waclawik, E.R., Du, A., 2016. Single Atom (Pd/Pt) Supported on Graphitic Carbon Nitride as an Efficient Photocatalyst for Visible-Light Reduction of Carbon Dioxide. *J Am Chem Soc* 138 (19), 6292–6297. <https://doi.org/10.1021/jacs.6b02692>.
- [17] Kumar, P., Vahidzadeh, E., Thakur, U.K., Kar, P., Alam, K.M., Goswami, A., et al., 2019. C₃N₅: A Low Bandgap Semiconductor Containing an Azo-Linked Carbon Nitride Framework for Photocatalytic, Photovoltaic and Adsorbent Applications. *J Am Chem Soc* 141 (13), 5415–5436. <https://doi.org/10.1021/jacs.9b00144>.
- [18] Liu, X., Hao, Z., Wang, H., Wang, T., Shen, Z., Zhang, H., et al., 2022. Enhanced localized dipole of Pt-Au single-site catalyst for solar water splitting. *Proceedings of the National Academy of Sciences* 119(8), e2119723119. <https://doi.org/10.1073/pnas.2119723119>.

- [19] Tong, J., Wang, D., Liu, Y., Lou, X., Jiang, J., Dong, B., et al., 2021. Bioinspired micro/nanomotor with visible light energy-dependent forward, reverse, reciprocating, and spinning schooling motion. *Proceedings of the National Academy of Sciences* 118(42), e2104481118. <https://doi.org/10.1073/pnas.2104481118>.
- [20] Van Viet, P., Nguyen, H.P., Tran, H.H., Bui, D.P., Hai, L.V., Pham, M.T., et al., 2021. Constructing g-C₃N₄/SnO₂ S-scheme heterojunctions for efficient photocatalytic NO removal and low NO₂ generation. *J Sci: Adv Mater Devices* 6(4), 551–559. <https://doi.org/10.1016/j.jsamd.2021.07.005>.
- [21] Yusuf, A., Sun, Y., Liu, S., Wang, C., Ren, Y., Xiao, H., et al., 2022. Study of the effect of ceria on the activity and selectivity of Co and Ce co-doped birnessite manganese oxide for formaldehyde oxidation. *J Hazard Mater* 424, 127583. <https://doi.org/10.1016/j.jhazmat.2021.127583>.
- [22] Chen, X., Huan, Y., Sun, N., Su, Y., Shen, X., Li, G., et al., 2023. Studying the variable energy band structure for energy storage materials in charge/discharge process. *Chin Chem Lett*, 108380. <https://doi.org/10.1016/j.ccl.2023.108380>.
- [23] Chen, Z., Liu, Z., Xu, X., 2023. Dynamic evolution of the active center driven by hemilabile coordination in Cu/CeO₂ single-atom catalyst. *Nat Commun* 14(1), 2512. <https://doi.org/10.1038/s41467-023-38307-w>.
- [24] Chen, Z., Wang, J., Hao, M., Xie, Y., Liu, X., Yang, H., et al., 2023. Tuning excited state electronic structure and charge transport in covalent organic frameworks for enhanced photocatalytic performance. *Nat Commun* 14(1), 1106. <https://doi.org/10.1038/s41467-023-36710-x>.
- [25] Jia, H., Du, A., Zhang, H., Yang, J., Jiang, R., Wang, J., et al., 2019. Site-Selective Growth of Crystalline Ceria with Oxygen Vacancies on Gold Nanocrystals for Near-Infrared Nitrogen Photofixation. *J Am Chem Soc* 141(13), 5083–5086. <https://doi.org/10.1021/jacs.8b13062>.
- [26] Nie, J., Zhu, G., Zhang, W., Gao, J., Zhong, P., Xie, X., et al., 2021. Oxygen vacancy defects-boosted deep oxidation of NO by β-Bi₂O₃/CeO₂-δ p-n heterojunction photocatalyst in situ synthesized from Bi/Ce(CO₃)(OH) precursor. *Chem Eng J* 424, 130327. <https://doi.org/10.1016/j.cej.2021.130327>.
- [27] Wang, S., Yao, W., Lin, J., Ding, Z., Wang, X., 2014. Cobalt Imidazolate Metal–Organic Frameworks Photosplit CO₂ under Mild Reaction Conditions. *Angew Chem Int Ed* 53(4), 1034–1038. <https://doi.org/10.1002/anie.201309426>.
- [28] Sahoo, D.P., Nayak, S., Reddy, K.H., Martha, S., Parida, K., 2018. Fabrication of a Co(OH)₂/ZnCr LDH “p–n” Heterojunction Photocatalyst with Enhanced Separation of Charge Carriers for Efficient Visible-Light-Driven H₂ and O₂ Evolution. *Inorg Chem* 57(7), 3840–3854. <https://doi.org/10.1021/acs.inorgchem.7b03213>.
- [29] Xu, H., Li, S., Ge, L., Han, C., Gao, Y., Dai, D., 2017. In-situ synthesis of novel plate-like Co(OH)₂ co-catalyst decorated TiO₂ nanosheets with efficient photocatalytic H₂ evolution activity. *Int J Hydrog Energy* 42(36), 22877–22886. <https://doi.org/10.1016/j.ijhydene.2017.07.186>.
- [30] Xu, S., Zhou, P., Zhang, Z., Yang, C., Zhang, B., Deng, K., et al., 2017. Selective oxidation of 5-hydroxymethylfurfural to 2,5-furandicarboxylic acid using O₂ and a photocatalyst of Co-thiophorpyrazine bonded to g-C₃N₄. *J Am Chem Soc* 139(41), 14775–14782. <https://doi.org/10.1021/jacs.7b08861>.
- [31] Yusuf, A., Sun, Y., Ren, Y., Snape, C., Wang, C., Jia, H., et al., 2020. Opposite effects of Co and Cu dopants on the catalytic activities of birnessite MnO₂ catalyst for low-temperature formaldehyde oxidation. *J Phys Chem C* 124(48), 26320–26331. <https://doi.org/10.1021/acs.jpcc.0c08508>.
- [32] Li, Z., Wu, Y., Lu, G., 2016. Highly efficient hydrogen evolution over Co(OH)₂ nanoparticles modified g-C₃N₄ co-sensitized by Eosin Y and Rose Bengal under Visible Light Irradiation. *Appl Catal B: Environ* 188, 56–64. <https://doi.org/10.1016/j.apcatb.2016.01.057>.
- [33] Xiao, F.-X., Zeng, Z., Liu, B., 2015. Bridging the Gap: Electron Relay and Plasmonic Sensitization of Metal Nanocrystals for Metal Clusters. *J Am Chem Soc* 137(33), 10735–10744. <https://doi.org/10.1021/jacs.5b06323>.
- [34] Ou, M., Wan, S., Zhong, Q., Zhang, S., Song, Y., Guo, L., et al., 2018. Hierarchical Z-scheme photocatalyst of g-C₃N₄@Ag/BiVO₄ (0 4 0) with enhanced visible-light-induced photocatalytic oxidation performance. *Appl Catal B: Environ* 221, 97–107. <https://doi.org/10.1016/j.apcatb.2017.09.005>.
- [35] Wei, L., Shengling, L., Chuanxiang, C., Ankang, C., 2016. Fabrication of TiO₂ / Ag / Ag₃PO₄ Heterostructured Nanorod Arrays on FTO for Enhanced Photoelectrochemical and Photocatalytic Performances, Proceedings of the 2016 3rd International Conference on Mechatronics and Information Technology. Atlantis Press, pp. 629–632.
- [36] Ezech, C.I., Tomatis, M., Yang, X., He, J., Sun, C., 2018. Ultrasonic and hydrothermal mediated synthesis routes for functionalized Mg–Al LDH: Comparison study on surface morphology, basic site strength, cyclic sorption efficiency and effectiveness. *Ultrason Sonochem* 40, 341–352. <https://doi.org/10.1016/j.ultrsonch.2017.07.013>.
- [37] Chu, C., Zhu, Q., Pan, Z., Gupta, S., Huang, D., Du, Y., et al., 2020. Spatially separating redox centers on 2D carbon nitride with cobalt single atom for photocatalytic H₂O₂ production. *Proc Natl Acad Sci* 117(12), 6376–6382. <https://doi.org/10.1073/pnas.1913403117>.
- [38] Shao, J., Zhang, J., Zhang, X., Feng, Y., Zhang, H., Zhang, S., et al., 2018. Enhance SO₂ adsorption performance of biochar modified by CO₂ activation and amine impregnation. *Fuel* 224, 138–146. <https://doi.org/10.1016/j.fuel.2018.03.064>.
- [39] Franchini, M., Philipsen, P.H.T., van Lenthe, E., Visscher, L., 2014. Accurate Coulomb Potentials for Periodic and Molecular Systems through Density Fitting. *J Chem Theory Comput* 10(5), 1994–2004. <https://doi.org/10.1021/ct500172n>.
- [40] Franchini, M., Philipsen, P.H.T., Visscher, L., 2013. The Becke Fuzzy Cells Integration Scheme in the Amsterdam Density Functional Program Suite. *J Comput Chem* 34(21), 1819–1827. <https://doi.org/10.1002/jcc.23323>.
- [41] Wiesenekker, G., Baerends, E.J., 1991. Quadratic integration over the three-dimensional Brillouin zone. *J Phys: Condens Matter* 3(35), 6721. <https://doi.org/10.1088/0953-8984/3/35/005>.
- [42] Han, H., Wang, X., Qiao, Y., Lai, Y., Liu, B., Zhang, Y., et al., 2023. Construction of S-scheme heterojunction for enhanced photocatalytic conversion of NO over dual-defect CeO_{2-x}/g-C₃N_{4-x}. *J Alloy Compd* 933, 167819. <https://doi.org/10.1016/j.jallcom.2022.167819>.
- [43] Han, S., Li, X., Tan, Y., Huang, Y., Wu, Z., Wang, M., et al., 2023. In-situ self-sacrificed fabrication of insulator-based SrTiO₃/SrCO₃ heterojunction interface for gaseous HCHO and NO photocatalytic degradation. *Appl Surf Sci* 612, 155806. <https://doi.org/10.1016/j.apsusc.2022.155806>.
- [44] Wang, S., Li, M., Gao, H., Yin, Z., Chen, C., Yang, H., et al., 2023. Construction of CeO₂/YMnO₃ and CeO₂/MgAl₂O₄/YMnO₃ photocatalysts and adsorption of dyes and photocatalytic oxidation of antibiotics: Performance prediction, degradation pathway and mechanism insight. *Appl Surf Sci* 608, 154977. <https://doi.org/10.1016/j.apsusc.2022.154977>.
- [45] Zhang, J., Shao, S., Zhou, D., Di, T., Wang, T., 2021. Two-Dimensional Layered Co(OH)₂/g-C₃N₄/Ni(OH)₂ Ternary Nanocomposites for Enhanced Visible-Light Photocatalytic H₂-Production Activity. *ACS Appl Energy Mater* 4(6), 6340–6347. <https://doi.org/10.1021/acsaem.1c01198>.
- [46] Zhang, Q., Xiao, W., Guo, W.H., Yang, Y.X., Lei, J.L., Luo, H.Q., et al., 2021. Macroporous Array Induced Multiscale Modulation at the Surface/Interface of Co(OH)₂/NiMo Self-Supporting Electrode for Effective Overall Water Splitting. *Adv Funct Mater* 31(33), 2102117. <https://doi.org/10.1002/adfm.202102117>.
- [47] Ye, Y.-X., Pan, J., Xie, F., Gong, L., Huang, S., Ke, Z., et al., 2021. Highly efficient photosynthesis of hydrogen peroxide in ambient conditions. *Proceedings of the National Academy of Sciences* 118(16), e2103964118. <https://doi.org/doi:10.1073/pnas.2103964118>.
- [48] Zhu, Z., Ni, Y., Lv, Q., Geng, J., Xie, W., Li, F., et al., 2021. Surface plasmon mediates the visible light-responsive lithium–oxygen battery with Au nanoparticles on defective carbon nitride. *Proceedings of the National Academy of Sciences* 118(17), e2024619118. <https://doi.org/doi:10.1073/pnas.2024619118>.
- [49] Zhang, X., Liang, H., Li, C., Bai, J., 2022. 1 D CeO₂/g-C₃N₄ type II heterojunction for visible-light-driven photocatalytic hydrogen evolution. *Inorg Chem Commun* 144, 109838. <https://doi.org/10.1016/j.inoche.2022.109838>.
- [50] Sabzehmeidani, M.M., Karimi, H., Ghaedi, M., 2022. Nanofibers based quaternary CeO₂/Co₃O₄/Ag/Ag₃PO₄ S-scheme heterojunction photocatalyst with enhanced degradation of organic dyes. *Mater Res Bull* 147, 111629. <https://doi.org/10.1016/j.materresbull.2021.111629>.
- [51] Gong, C., Zhao, L., Li, D., He, X., Chen, H., Du, X., et al., 2023. In-situ interfacial engineering of Co(OH)₂/Fe₇Se₈ nanosheets to boost electrocatalytic water splitting. *Chem Eng J* 466, 143124. <https://doi.org/10.1016/j.cej.2023.143124>.
- [52] Prajapati, P.K., Malik, A., Nandal, N., Pandita, S., Singh, R., Bhandari, S., et al., 2022. Morphology controlled Fe and Ni-doped CeO₂ nanorods as an excellent heterojunction photocatalyst for CO₂ reduction. *Appl Surf Sci* 588, 152912. <https://doi.org/10.1016/j.apsusc.2022.152912>.
- [53] Wu, D., Zhang, X., Liu, S., Ren, Z., Xing, Y., Jin, X., et al., 2022. Fabrication of a Z-scheme CeO₂/Bi₂O₄ heterojunction photocatalyst with superior visible-light responsive photocatalytic performance. *J Alloy Compd* 909, 164671. <https://doi.org/10.1016/j.jallcom.2022.164671>.
- [54] Zheng, L., Zhao, Y., Xu, P., Pan, Y., Yang, P., Wang, H.E., et al., 2022. Copper doped Co_x/Co(OH)₂ hierarchical mesoporous nanosheet arrays as binder-free electrodes for superior supercapacitors. *J Alloy Compd* 911, 165115. <https://doi.org/10.1016/j.jallcom.2022.165115>.
- [55] Fu, M., Hu, X., Wang, C., Lu, P., Bai, J., Wang, R., et al., 2022. Constructing a novel NaLa(WO₄)₂/g-C₃N₄ Z-scheme heterojunction with efficient carrier separation for excellent photocatalytic purification of NO. *J Alloy Compd* 906, 164371. <https://doi.org/10.1016/j.jallcom.2022.164371>.
- [56] Geng, Y., Chen, D., Li, N., Xu, Q., Li, H., He, J., et al., 2021. Z-Scheme 2D/2D α-Fe₂O₃/g-C₃N₄ heterojunction for photocatalytic oxidation of nitric oxide. *Appl Catal B: Environ* 280, 119409. <https://doi.org/10.1016/j.apcatb.2020.119409>.
- [57] Tan, Y., Wei, S., Liu, X., Pan, B., Liu, S., Wu, J., et al., 2021. Neodymium oxide (Nd₂O₃) coupled tubular g-C₃N₄, an efficient dual-function catalyst for photocatalytic hydrogen production and NO removal. *Sci Total Environ* 773, 145583. <https://doi.org/10.1016/j.scitotenv.2021.145583>.
- [58] Razzaq, R., Zhu, H., Jiang, L., Muhammad, U., Li, C., Zhang, S., 2013. Catalytic Methanation of CO and CO₂ in Coke Oven Gas over Ni–Co/ZrO₂–CeO₂. *Ind Eng Chem Res* 52(6), 2247–2256. <https://doi.org/10.1021/ie301399z>.
- [59] Tang, Y., Yang, Y., Cheng, D., Gao, B., Wan, Y., Li, Y.C., 2017. Value-Added Humic Acid Derived from Lignite Using Novel Solid-Phase Activation Process with Pd/CeO₂ Nanocatalyst: A Physicochemical Study. *ACS Sustain Chem Eng* 5(11), 10099–10110. <https://doi.org/10.1021/acssuschemeng.7b02094>.
- [60] Zhu, C., Wang, Y., Jiang, Z., Xu, F., Xian, Q., Sun, C., et al., 2019. CeO₂ nanocrystal-modified layered MoS₂/g-C₃N₄ as OD/2D ternary composite for visible-light photocatalytic hydrogen evolution: Interfacial consecutive multi-step electron transfer and enhanced H₂O reactant adsorption. *Appl Catal B: Environ* 259, 118072. <https://doi.org/10.1016/j.apcatb.2019.118072>.
- [61] Zhou, X., Jin, J., Zhu, X., Huang, J., Yu, J., Wong, W.Y., et al., 2016. New Co(OH)₂/CdS nanowires for efficient visible light photocatalytic hydrogen production. *J Mater Chem A* 4(14), 5282–5287. <https://doi.org/10.1039/C6TA00325G>.
- [62] Gan, J., Wang, H., Hu, H., Su, M., Chen, F., Xu, H., 2021. Efficient synthesis of tunable band-gap CuInZnS decorated g-C₃N₄ hybrids for enhanced CO₂ photocatalytic reduction and near-infrared-triggered photodegradation performance. *Appl Surf Sci* 564, 150396. <https://doi.org/10.1016/j.apsusc.2021.150396>.

- [63] Huang, Y.-C., Wu, S.-H., Hsiao, C.-H., Lee, A.-T., Huang, M.H., 2020. Mild Synthesis of Size-Tunable CeO₂ Octahedra for Band Gap Variation. *Chem Mater* 32 (6), 2631–2638. <https://doi.org/10.1021/acs.chemmater.0c00318>.
- [64] Wang, L., Fang, Z., Qi, T., Xing, L., Liu, J., Zhang, S., et al., 2020. Short-range ordered Co(OH)₂/TiO₂ for boosting sulfite oxidation: Performance and mechanism. *J Colloid Interface Sci* 571, 90–99. <https://doi.org/10.1016/j.jcis.2020.03.042>.
- [65] Duan, L., Li, G., Zhang, S., Wang, H., Zhao, Y., Zhang, Y., 2021. Preparation of S-doped g-C₃N₄ with C vacancies using the desulfurized waste liquid extracting salt and its application for NO_x removal. *Chem Eng J* 411, 128551. <https://doi.org/10.1016/j.cej.2021.128551>.
- [66] Feizpoor, S., Habibi-Yangjeh, A., Vadel, S., 2017. Novel TiO₂/Ag₂CrO₄ nanocomposites: Efficient visible-light-driven photocatalysts with n-n heterojunctions. *J Photochem Photobiol A: Chem* 341, 57–68. <https://doi.org/10.1016/j.jphotochem.2017.03.028>.
- [67] Wang, Z., Lin, Z., Shen, S., Zhong, W., Cao, S., 2021. Advances in designing heterojunction photocatalytic materials. *Chin J Catal* 42 (5), 710–730. [https://doi.org/10.1016/S1872-2067\(20\)63698-1](https://doi.org/10.1016/S1872-2067(20)63698-1).
- [68] Yan, Y., Guan, H., Liu, S., Jiang, R., 2014. Ag₃PO₄/Fe₂O₃ composite photocatalysts with an n-n heterojunction semiconductor structure under visible-light irradiation. *Ceram Int* 9095–9100. <https://doi.org/10.1016/j.ceramint.2014.01.123>.
- [69] Geng, J., Zhao, L., Wang, M., Dong, G., Ho, W., 2022. The photocatalytic NO-removal activity of g-C₃N₄ significantly enhanced by the synergistic effect of Pd⁰ nanoparticles and N vacancies. *Environ Sci: Nano* 9 (2), 742–750. <https://doi.org/10.1039/D1EN00937K>.
- [70] Li, F., Liu, G., Liu, F., Wu, J., Yang, S., 2023. Synergetic effect of CQD and oxygen vacancy to TiO₂ photocatalyst for boosting visible photocatalytic NO removal. *J Hazard Mater* 452, 131237. <https://doi.org/10.1016/j.jhazmat.2023.131237>.
- [71] Li, K., Zhou, W., Li, X., Li, Q., Carabineiro, S.A.C., Zhang, S., et al., 2023. Synergistic effect of cyano defects and CaCO₃ in graphitic carbon nitride nanosheets for efficient visible-light-driven photocatalytic NO removal. *J Hazard Mater* 442, 130040. <https://doi.org/10.1016/j.jhazmat.2022.130040>.
- [72] Li, X., Li, K., Ding, D., Yan, J., Wang, C., Carabineiro, S.A.C., et al., 2023. Effect of oxygen vacancies on the photocatalytic activity of flower-like BiOBr microspheres towards NO oxidation and CO₂ reduction. *Sep Purif Technol* 309, 123054. <https://doi.org/10.1016/j.seppur.2022.123054>.
- [73] Li, X., Zhao, R., Li, H., Jiang, J., Ai, L., Cao, X., et al., 2023. Constructing the multilayer O-g-C₃N₄@W₁₈O₄₉ heterostructure for deeply photocatalytic oxidation NO. *Sep Purif Technol* 307, 122841. <https://doi.org/10.1016/j.seppur.2022.122841>.
- [74] Qi, Z., Chen, J., Zhou, W., Li, Y., Li, X., Zhang, S., et al., 2023. Synergistic effects of holey nanosheet and sulfur-doping on the photocatalytic activity of carbon nitride towards NO removal. *Chemosphere* 316, 137813. <https://doi.org/10.1016/j.chemosphere.2023.137813>.
- [75] Xin, Y., Zhu, Q., Gao, T., Li, X., Zhang, W., Wang, H., et al., 2023. Photocatalytic NO removal over defective Bi/BiOBr nanoflowers: The inhibition of toxic NO₂ intermediate via high humidity. *Appl Catal B: Environ* 324, 122238. <https://doi.org/10.1016/j.apcatb.2022.122238>.
- [76] Liu, J., 2015. Origin of High Photocatalytic Efficiency in Monolayer g-C₃N₄/CdS Heterostructure: A Hybrid DFT Study. *J Phys Chem C* 119 (51), 28417–28423. <https://doi.org/10.1021/acs.jpcc.5b09092>.
- [77] Mirsadeghi, S., Ghoreishian, S.M., Zandavar, H., Behjatmanesh-Ardakani, R., Naghian, E., Ghoreishian, M., et al., 2023. In-depth insight into the photocatalytic and electrocatalytic mechanisms of Mg₃V₂O₈@Zn₃V₂O₈@ZnO ternary heterostructure toward linezolid: Experimental and DFT studies. *J Environ Chem Eng* 11 (1), 109106. <https://doi.org/10.1016/j.jece.2022.109106>.
- [78] Samsudin, M.F.R., Ullah, H., Tahir, A.A., Li, X., Ng, Y.H., Sufian, S., 2021. Superior photoelectrocatalytic performance of ternary structural BiVO₄/GQD/g-C₃N₄ heterojunction. *J Colloid Interface Sci* 586, 785–796. <https://doi.org/10.1016/j.jcis.2020.11.003>.
- [79] She, S., Zhang, X., Wu, X., Li, J., Zhang, G., 2021. The fabrication of two-dimensional g-C₃N₄/NaBiO₃·2H₂O heterojunction for improved photocatalytic CO₂ reduction: DFT study and mechanism unveiling. *J Colloid Interface Sci* 604, 122–130. <https://doi.org/10.1016/j.jcis.2021.06.169>.
- [80] Shen, J., Qian, L., Huang, J., Guo, Y., Zhang, Z., 2021. Enhanced degradation toward Levofloxacin under visible light with S-scheme heterojunction In₂O₃/Ag₂CO₃: Internal electric field, DFT calculation and degradation mechanism. *Sep Purif Technol* 275, 119239. <https://doi.org/10.1016/j.seppur.2021.119239>.
- [81] Xu, D., Cheng, B., Wang, W., Jiang, C., Yu, J., 2018. Ag₂CrO₄/g-C₃N₄/graphene oxide ternary nanocomposite Z-scheme photocatalyst with enhanced CO₂ reduction activity. *Appl Catal B: Environ* 231, 368–380. <https://doi.org/10.1016/j.apcatb.2018.03.036>.